



HAL
open science

Advanced characterization of soot precursors via excitation emission matrices fluorescence spectroscopy and molecular modeling

Jessy Elias, Luc Labarriere, Alessandro Faccinetto, Aurélien Moncomble,
Jean-Paul Cornard, Xavier Mercier

► To cite this version:

Jessy Elias, Luc Labarriere, Alessandro Faccinetto, Aurélien Moncomble, Jean-Paul Cornard, et al.. Advanced characterization of soot precursors via excitation emission matrices fluorescence spectroscopy and molecular modeling. Carbon, 2024, Carbon, 228, pp.119355. 10.1016/j.carbon.2024.119355 . hal-04676344

HAL Id: hal-04676344

<https://hal.univ-lille.fr/hal-04676344v1>

Submitted on 8 Nov 2024

HAL is a multi-disciplinary open access archive for the deposit and dissemination of scientific research documents, whether they are published or not. The documents may come from teaching and research institutions in France or abroad, or from public or private research centers.

L'archive ouverte pluridisciplinaire **HAL**, est destinée au dépôt et à la diffusion de documents scientifiques de niveau recherche, publiés ou non, émanant des établissements d'enseignement et de recherche français ou étrangers, des laboratoires publics ou privés.

Advanced Characterization of Soot Precursors via Excitation Emission Matrices Fluorescence Spectroscopy and Molecular Modeling

Authors: J. Elias^{1,2}, L. Labarrière³, A. Faccinetto¹, A. Moncomble³, J.-P. Cornard³, X. Mercier^{1*}

Affiliations:

¹Université Lille, CNRS, UMR 8522 - PC2A - Physicochimie des Processus de Combustion et de l'Atmosphère, F-59000 Lille, France

²French Environment and Energy Management Agency, Angers, France

³Université Lille, CNRS, UMR 8516 - LASIRE - Laboratoire de Spectroscopie pour les Interactions, la Réactivité et l'Environnement, F-59000 Lille, France,

*Correspondence to: Xavier Mercier (xavier.mercier@univ-lille.fr). Tel: + 33 3 20 33 64 69

Highlights:

- Implementation of an innovative optical method to characterize soot precursors
- New insights into various aromatic species characterizing soot precursors in flames
- Bridging the gap between gaseous precursors and solid soot in the inception stage
- Theoretical calculations to interpret spectra and identify key species initiating soot formation

Abstract

Particulate emissions generated from combustion processes of hydrocarbon fuels (soot) have become a significant environmental issue with implications for both human health and climate change. However, soot particles also offer exciting possibilities in the field of carbonaceous nanomaterials which have found applications in optoelectronics, bioimaging, drug delivery, and photocatalysis. This study aims to investigate the species implicated in the initial steps of soot particle formation characterized by the transformation of gaseous precursors, like polycyclic aromatic hydrocarbons (PAHs), into soot particles in the condensed phase. While PAHs have been long known to be soot precursors, recent researches suggest that resonance-stabilized radical (RSR) aromatic compounds may play a substantial role in this process. To shed light on this process, we conducted a series of experiments in a laminar diffusion sooting flame in controlled laboratory conditions, notably by implementing the excitation-emission matrix (EEM) method to study the optical properties of soot precursors. This innovative approach provides critical insights into the involvement of various kinds of aromatic species during the early steps of soot formation. In parallel with the experimental work, theoretical calculations were carried out to determine the spectral features of PAHs, PAH dimers, and resonance-stabilized PAH radicals. These calculations support the interpretation of the fluorescence EEM and assist the identification of species at the origin of soot inception. These findings contribute to a deeper understanding of the interplay between PAHs and persistent radicals, particularly at the onset of soot formation within flames.

Keywords: Soot inception, excitation-emission matrix, laser induced fluorescence, polycyclic aromatic hydrocarbons, resonance-stabilized radicals, DFT calculations

1. Introduction

Soot particle emissions arising from combustion processes have become a global concern, particularly in urban environments and regions with high levels of industrial and vehicular activities. Soot particles have been linked to several health pathologies, spanning cardiovascular diseases, respiratory allergies, and lung cancer [1–4]. Furthermore, soot particles released in the environment also impact the climate change because of their significant radiative forcing [5,6]. Addressing soot formation becomes critical for air quality management. In particular, the ability to identify the soot molecular precursors and control the mechanisms of soot formation offers a pathway toward reducing the health risks and environmental issues associated with fine particulate matter.

On the other hand, soot particles are increasingly implicated in the design of new carbonaceous nanomaterials. Nanocarbon dots, also known as carbon quantum dots (CDs), are a recent addition to the carbon nanomaterial family [7,8]. These carbon nanoparticles exhibit unique properties [9–11], including tunable photoluminescence, exceptional chemical stability, and biocompatibility that led to applications in numerous fields [12–14] as diverse as optoelectronics, bioimaging, drug delivery, and photocatalysis.

Consequently, the study of soot formation and the characterization of the molecular precursors as well as the chemical pathways leading to soot particles is essential both for understanding the environmental and health impact of the combustion emissions, but also to better apprehend the possibilities of developments and applications in the field of carbonaceous nanomaterials. In that context, the soot inception step, i.e. the transformation of gaseous molecular precursors like polycyclic aromatic hydrocarbons (PAHs) or their derivatives into soot particles in the condensed phase, is not yet clarified [15–19]. Although the implication of PAHs as soot

precursors is well established, the process of transforming gaseous PAHs into soot particles in the condensed phase is far from straightforward and is marked by intricate physicochemical mechanisms and the involvement of a diverse range of reactive species [20–23]. Small to moderate sized PAHs, typically represented by naphthalene to coronene, are usually considered as the main PAHs implicated in soot inception [16,21]. However, the physicochemical processes allowing these species to form 3D molecular edifices is still not yet well understood. Although van der Waals dimerization of PAHs has long been suggested and is still used in some kinetics models to represent the inception step, the weakness of the resulting electrostatic bonds has been shown to be not strong enough to allow PAH dimers to survive at flame temperature [16,24]. To solve this issue, the stabilization of PAH dimers through formation of covalent C-C bonds has been suggested by different works [18,23,25,26] and further supported by experimental investigations that highlighted the formation of aliphatic bridges between PAHs [27]. The formation of such structures and their growth into 3D clusters of crosslinked PAHs constituting the amorphous core of the incipient soot particles are currently expected to involve PAH radicals [21,28–33]. Frenklach and Mebel [23,34] notably proposed the formation of E-bridge PAHs according to chemical pathways essentially driven by the HACA mechanism and implicating the formation of a rotationally-activated dimer by the collision of aromatic molecule and an aromatic radical. Johansson et al. [28] suggested the implication of rapid molecular clustering–reaction pathways involving resonance-stabilized radical (RSR) chain reactions to initiate the particle formation. Martin et al. [29] characterized the capability and propensity of bonding of several types of PAH radicals with other radicals, and demonstrated that they could form strongly bound complexes, suggesting a significant role in soot formation. In particular, in a recent paper, Selvakumar et al. [35] reported a study of the role of π -radical localization on the transformation

of gas-phase aromatics into condensed phase particles by characterizing the possibilities of bonding of delocalized and localized π -radicals.

In parallel to these theoretical works, a few emerging research works reported experimental evidences of the existence of RSR PAHs in samples extracted from sooting flames by electron paramagnetic resonance (EPR) [32,36,37] and high-resolution atomic force microscopy (AFM) [25,30]. These studies notably reported the identification in incipient soot of fused six-membered aromatic rings partially substituted with aliphatic chains as well as compounds containing five-member rings on their periphery. The reported kind of species has been corroborated by recent pulsed EPR experiments [37] that revealed highly branched, resonance-stabilized aromatic radicals bearing aliphatic groups, reaching their maximum spin concentration in the inception region of a laminar diffusion sooting flame.

In this work, we carried out a series of experiments in a laminar sooting diffusion flame to provide new experimental data enabling to advance the characterization of the species involved in the soot inception step. This flame has been selected for the stratified distribution of different classes of species along its vertical central axis. Previous works [38,39] showed by in situ optical measurements and ex situ chemical analysis that the species formed along the height above the burner (HAB) are representative of the different steps of the soot formation, and highlighted three main regions along this axis, characteristic of the condensable gas, incipient soot, and mature soot. The whole reported study was carried out by employing laser-induced fluorescence (LIF) enabling the determination of excitation-emission matrices (EEM). This method relies on collecting emission fluorescence spectra for different excitation wavelengths and assembling them into matrices as a function of the excitation and emission wavelength. This method allows the fine examination of the optical properties of soot and molecular precursors, offering insights

into the presence of various kind of species. The interpretation of the EEM was assisted by theoretical calculations of spectral features at the DFT level of theory of PAHs, dimers of PAHs and RSR PAHs. This combined theoretical-experimental approach aimed to bridge the gap between the gaseous precursors and the soot particles in the condensed phase, providing critical information about the species involved in soot inception.

2. Experimental Methodology

2.1 Flame and burner

Measurements were performed on the 120 mm high, co-flow, laminar diffusion flame of methane stabilized on a Gülder-type burner at atmospheric pressure already described in details elsewhere [37,40]. This burner consists of a central injector supplied with 0.52 L min^{-1} of methane and surrounded by 86.6 L min^{-1} air flow (standard p and T). The flame is characterized by a partially stratified distribution of PAHs and soot in the centerline that allows measurements at different heights above the burner (HAB) to monitor the soot formation process. A picture of the flame is reported in the appendices (**Figure A.1**).

2.2 Optical setup

The scheme of the experimental setup used for the LIF measurements, which subsequently allows the determination of the EEM, is shown in **Figure 1**.

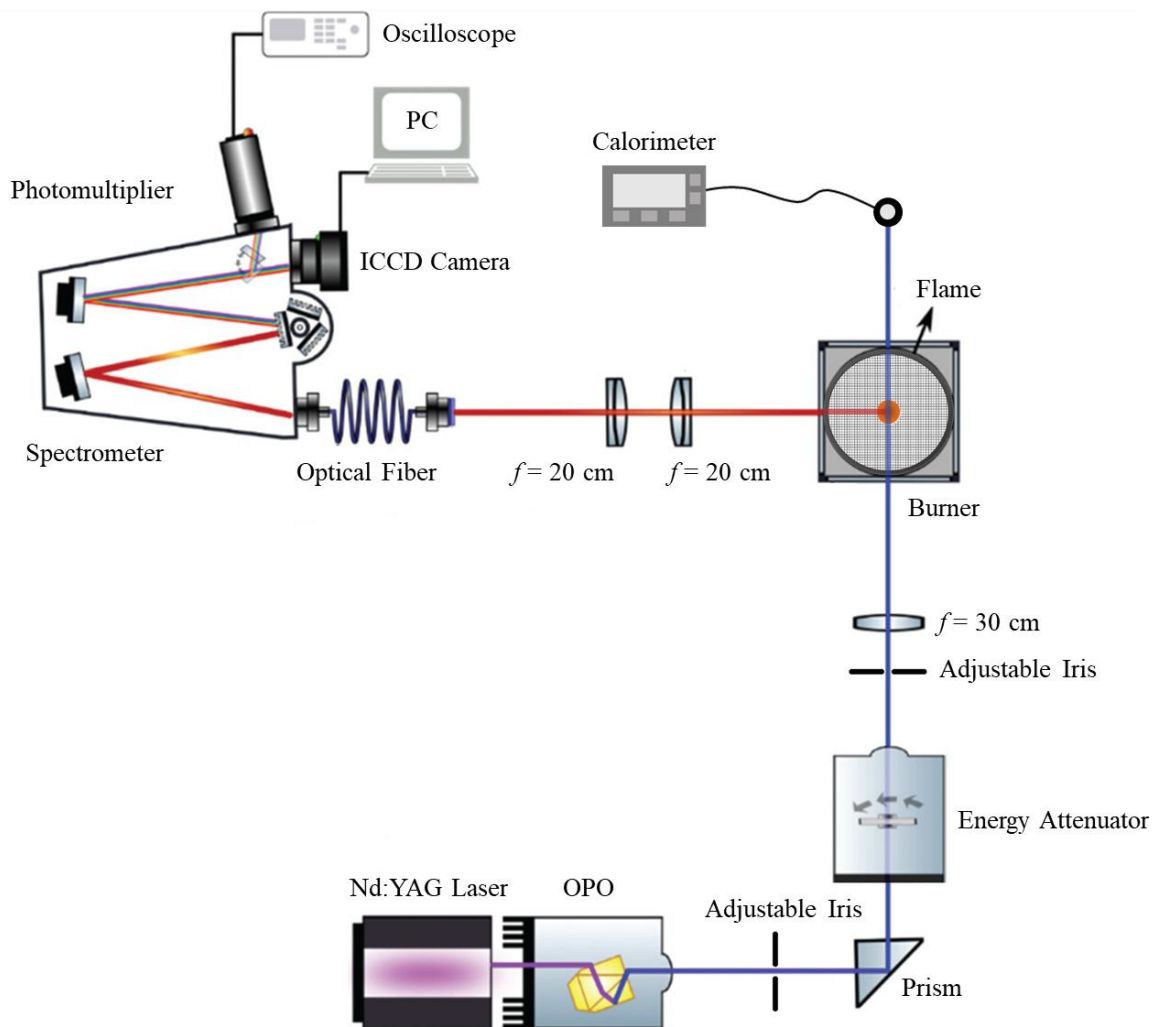


Figure 1: Schematic of the LIF measurements setup

The excitation source used for the LIF analyses consists of a Nd:YAG laser (Quanta-ray, Spectra Physics) generating laser pulses at 1064, 532, and 355 nm (6 ns pulse width, 10 Hz repetition rate) that are mixed and used to pump an optical parametric oscillator (OPO - premiScan-ULD/240, GWU-Lasertechnik) allowing the generation of tunable laser pulses over a wide spectral range from 210 nm to 2 μ m. Fourteen different excitation wavelengths (215, 220, 230, 240, 250, 265, 280, 290, 370, 405, 488, 532, 594, and 658 nm) were used for these experiments. For each of these wavelengths, fluorescence emission spectra were recorded all

along the flame height, every 2.5 mm at low HAB (10-20 mm) and then every 5 mm up to 90 mm HAB, to provide a sufficient spatial resolution for the analysis of the fluorescence EEM. A variable energy attenuator was positioned before the flame to control the energy of the laser beam. The purpose of this control was mainly to limit the laser energy used for the LIF measurements in order to fulfill the requirements for the linear energy regime and to avoid the activation of the laser induced incandescence (LII) process due to the presence of soot particles above 60 mm HAB. A laser energy of 15 $\mu\text{J}/\text{pulse}$ was defined for all LIF measurements. The laser beam was focused at the center of the flame with a spherical lens ($f = 300$ mm). The laser beam was characterized by a gaussian beam shape with a beam waist diameter estimated around 500 μm at the focus point in the flame. A calorimeter was installed behind the flame to control the laser energy during the experiments.

The emitted fluorescence was collected at right angle with two spherical lenses (200 mm focal length and 50 mm diameter). The collected fluorescence was transmitted, by means of a 1.25 mm diameter bundle of 19 optical fibers of 200 μm diameter (model LG-455-020) to a spectrometer (IHR320, Jobin Yvon) equipped with a 100 grooves/mm grating blazed at 450 nm. The spectrometer was coupled to a PI-MAX2 Roper Scientific intensified charge-coupled device (ICCD) camera for the acquisition of fluorescence spectra, featuring an RB (red-blue) Gen II intensifier. As shown below, the recorded fluorescence spectra upon UV excitation were systematically shifted towards higher UV/visible wavelengths regarding of the excitation wavelength. Hence, to limit interference from laser scattering, different high-pass filters at 280 nm, 295 nm and 305 nm were used to remove the excitation wavelengths respectively below 265 nm, 280 nm, and 290 nm. Above 370 nm, the excitation wavelengths were always included in the fluorescence emission spectra requiring in this case specific notch filters to suppress the

intense scattering signal from the fluorescence emission spectra. Hence, notch filters centered at wavelengths 370 nm, 405 nm, 488 nm, 532 nm, 594 nm, and 658 nm were used in this case. Two positions of the spectrometer were defined to cover the entire PAH fluorescence emission spectral range from 280 to 840 nm. The natural emission from the flame was collected at each HAB and subtracted from the corresponding fluorescence spectra. The fluorescence emission spectra were finally corrected from the transmission function of the detection system, determined separately thanks to a calibrated halogen/deuterium lamp.

3. EEM fluorescence spectroscopy

3.1 Description of the EEM method

In this study, we developed and implemented a methodology for the interpretation of LIF spectra based on the use of the excitation-emission matrix (EEM). LIF is a well-established measurement technique for combustion-related research that finds extensive application in the analysis of PAHs in flames [39,41–45]. Various research groups have conducted comprehensive examinations of fluorescence spectra obtained with diverse excitation wavelengths, spanning from UV to visible regions [22,39,42,46,47]. Owing to the distinct spectroscopic characteristics of PAHs, this technique enables the identification of PAH classes formed in flames. PAH monomer spectroscopy primarily involves π - π^* transitions, characterized by prominent absorption bands in the UV range 200-300 nm, which shift and broaden toward longer wavelengths as the size of the aromatic system increases. Consequently, the fluorescence emission spectra of these species exhibit emission bands typically in the 300-450 nm spectral range. By shifting the excitation wavelength to the visible, the fluorescence of larger PAHs can be detected. Consequently, it was demonstrated that the identification of PAH classes can be accomplished by adjusting the excitation wavelength. In the literature, the analysis of

fluorescence spectra obtained under UV excitation in flames is typically conducted by considering distinct spectral ranges, ascribed to the emission of various PAH classes [48,49]. The commonly accepted classification goes as follows: small PAHs with 2 or 3 aromatic rings are considered to fluoresce in the range 320-380 nm, while larger PAHs with 4 or more aromatic rings are expected to fluoresce above 400 nm. Although this approach permits a rough differentiation of PAH classes based on the size of the aromatic structure, it only provides a limited interpretation of the fluorescence spectra, primarily due to the potential overlap of different spectral contributions from the species generated in the flames

The EEM allows a richer interpretation of the LIF data and a finer identification of the spectral structures of the species formed in the flame than the classical methodology based on a single excitation wavelength. The EEM was first introduced by Johnson et al. [50] in the 1970s to analyze multi-component fluorescence based on the spectral information contained in the emission and excitation spectra of each luminescent species. The intensity of the fluorescence emission signal measured during a LIF experiment depends on both the excitation wavelength λ_{exc} and the emission wavelength λ_{em} . If λ_{exc} is held constant and λ_{em} is scanned, a fluorescence emission spectrum is obtained. Conversely, if λ_{em} is held constant while λ_{exc} is scanned, a fluorescence excitation spectrum is obtained. The EEM is the plot of the fluorescence intensity against λ_{em} against λ_{exc} . EEM fluorescence spectroscopy is now commonly used for the analysis and identification of specific compounds in complex mixtures in various experimental contexts. Implementations of this method are notably reported for the detection of PAHs [51,52] or the direct characterization of fuel components [53]. In combustion research, Aizawa et al. [54] used EEM fluorescence spectroscopy to study soot precursors in diesel spray flames using four different excitation wavelengths (266, 299, 342 and 398 nm) in the UV spectral range.

In this work, we implemented the EEM fluorescence spectroscopy to characterize the aromatic precursors formed in the flame during soot formation with an optimized spectral resolution relying on 14 different excitation wavelengths selected in the UV-visible spectral range. At each HAB, one EEM was obtained, consisting of a matrix of the fluorescence emission spectra recorded in the spectral range 280-840 nm for each of the 14 different excitation wavelengths.

A linear interpolation function was used with Matlab® to obtain 765×444 pixels resolution arrays having spectral resolution comparable with the resolution of the EEM determined for pure PAHs discussed in the next section.

3.2 Determination of the reference EEM of pure PAHs

To assist the interpretation of the flame EEM, reference EEMs of several pure PAHs expected to form in sooting flames were first built. An illustration of the method used to obtain these reference EEMs is reported in the appendices (**Figure A.2**). Basically, the EEM of pure PAHs is obtained using the absorption and emission spectra available in the literature. Each element of the matrix EEM_{ij} was calculated as:

$$EEM_{ij} = I(\lambda_{em})_i \times I(\lambda_{exc})_j \quad (\text{eq. 1})$$

where $I(\lambda_{em})_i$ is the intensity of the fluorescence emission spectrum at the wavelength λ_{em} and $I(\lambda_{exc})_j$ is the intensity of the fluorescence excitation spectrum at the wavelength λ_{exc} . The emission and the excitation spectra are both normalized to their maximum intensity in the investigated spectral range. As illustrated in **Figure A.2** for anthracene and fluoranthene, even though these two PAHs have fairly close absorption and emission spectral features, their EEMs are sufficiently different to enable their selective identification.

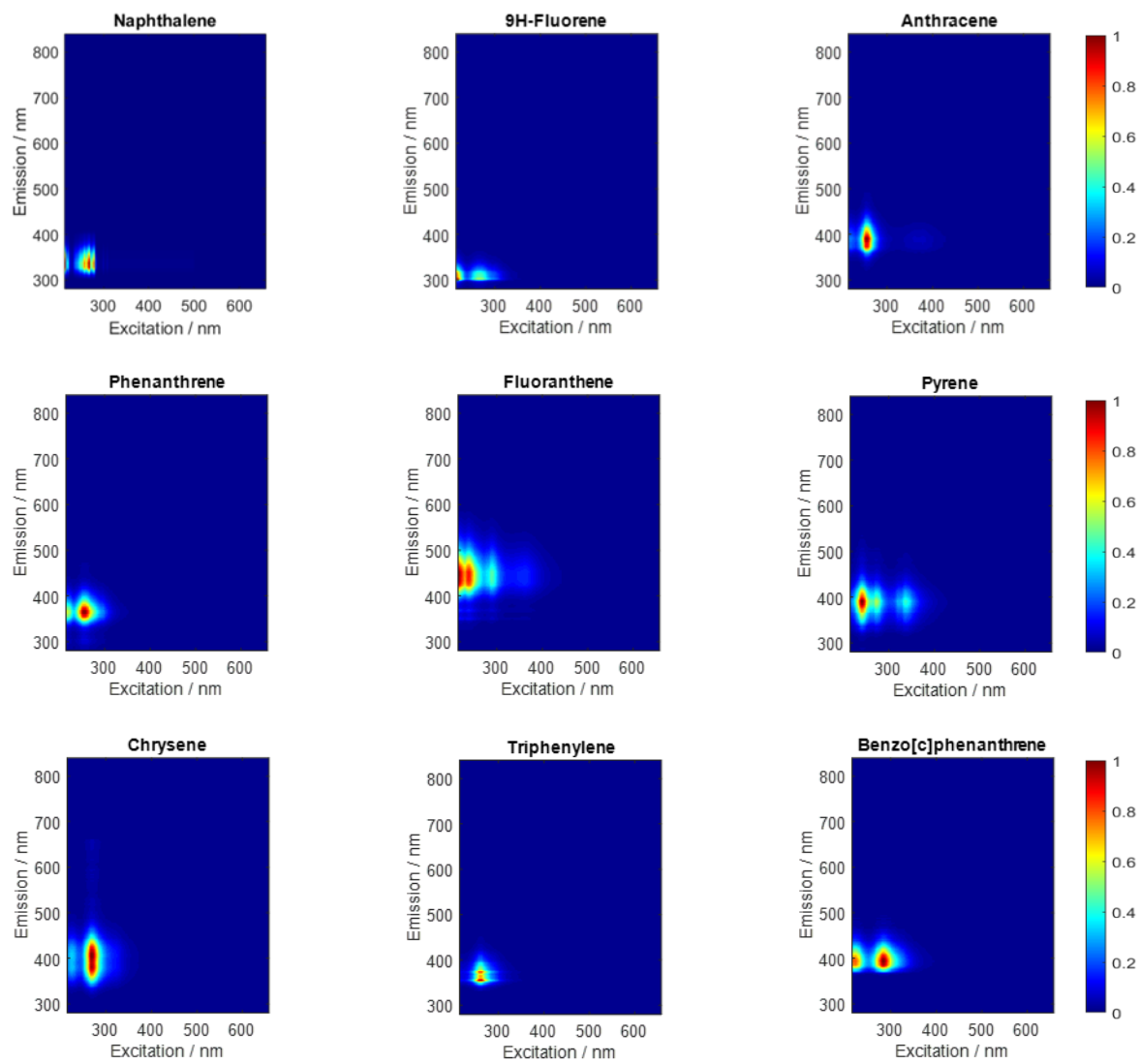
In this work, we considered a set of 15 PAHs ranging from naphthalene (2 aromatic rings) to coronene (7 aromatic rings) as representative of the main aromatic classes and structures

expected to be involved in soot inception [16]. It should be noted that for the construction of the reference EEMs, substituted PAHs were not considered (e.g., with side chains, or containing heteroatoms like oxygen and nitrogen). Although substituted PAHs are known to form in sooting flames, the low spectral resolution of the LIF at flame temperature does not enable an accurate distinction of the slight spectral shifts induced by the substitution. The complete list of the selected PAHs and associated reference publications for the excitation and emission fluorescence spectra used to build the reference EEMs can be found in the appendices (**table A.1**).

At flame temperature, a significant number of molecules occupy higher vibronic levels than at room temperature that results in the red shift of the absorption bands because of the lower photon energy necessary to excite these new transitions between vibronic states. Moreover, the red shift of the spectra is generally associated to the broadening and intensity decrease of the peaks. Hence, in order to define EEM fitting our experimental flame conditions, we used the absorption spectra determined by Bauer et al. [55] at 1750 K according to a methodology relying on the convolution of absorption spectra recorded at room temperature with a simplified Maxwell-Boltzmann distribution model. In this work, the absorption spectra of the considered PAHs were not recalculated at each flame temperature, but rather an average constant flame temperature of 1750 K was used for all the spectra. This approximation is based on the same work by Bauer et al. [55], in which the authors found that at elevated temperature around 1750 K, variations of about 200 K only have a minor impact on the structure of the simulated absorption spectra. [The impact of the variation of the temperature in the investigate flame conditions on the shape of the absorption spectra was also considered as negligible.](#)

Regarding the emission spectra used to build the reference EEMs, when available we used the emission spectra of pure PAHs recorded by Karcher et al. [56,57] at room temperature and

mostly in solution. Due to the Kasha's rule [58,59], the emission spectra of PAHs are only barely affected by the temperature. This is due to the fact that the fluorescence photons following laser excitation are mainly emitted from the lowest vibrational level of the first excited electronic level due to internal energy redistribution processes taking place before the radiative relaxation of the excited species [60,61]. Thus, the structure of the fluorescence emission spectra of PAHs remains essentially unaffected by the excitation wavelength and the temperature conditions. Nevertheless, high-temperature fluorescence emission spectra of PAHs were used whenever available in the literature. The reference EEMs of the individual PAHs determined this way are shown in **Figure 2** where the relative intensity (represented in colormaps) is normalized for each image.



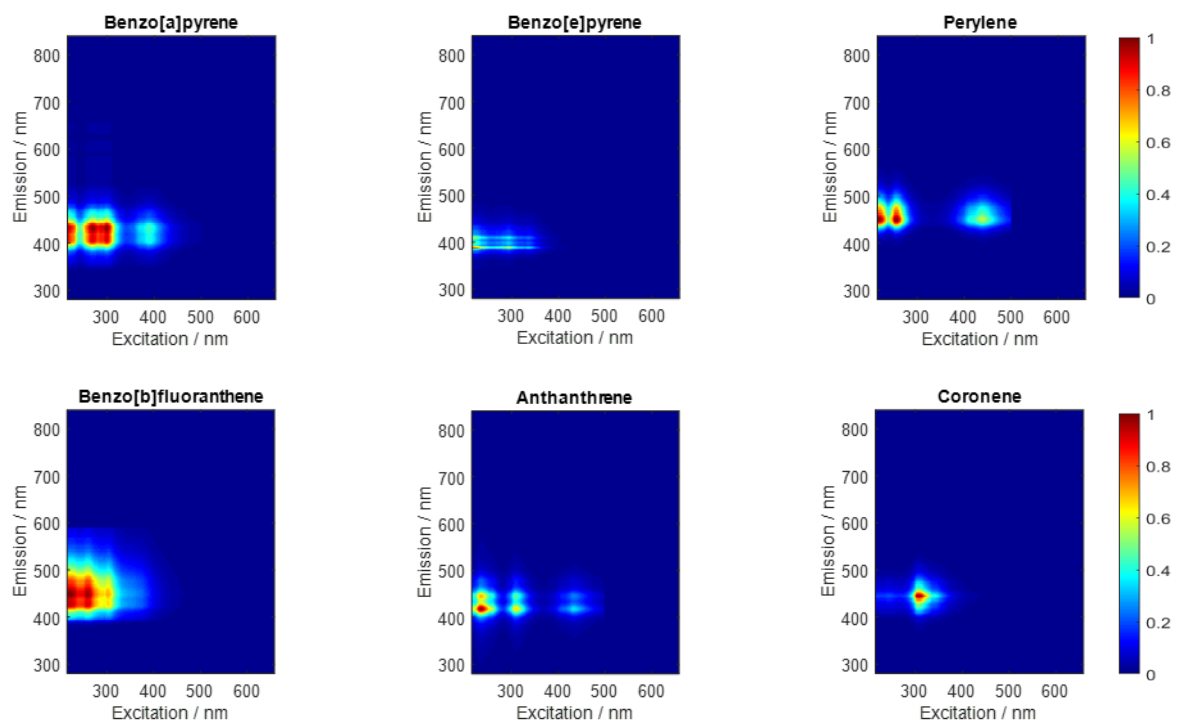


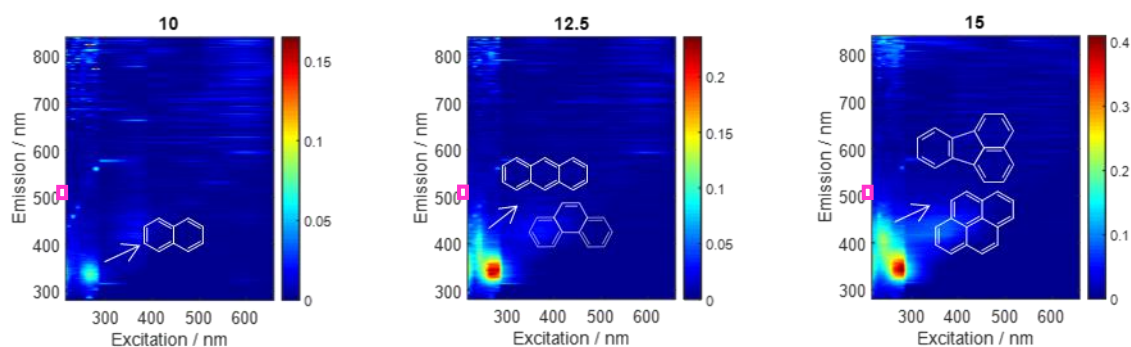
Figure 2: Reference EEMs of selected PAHs at 1750 K

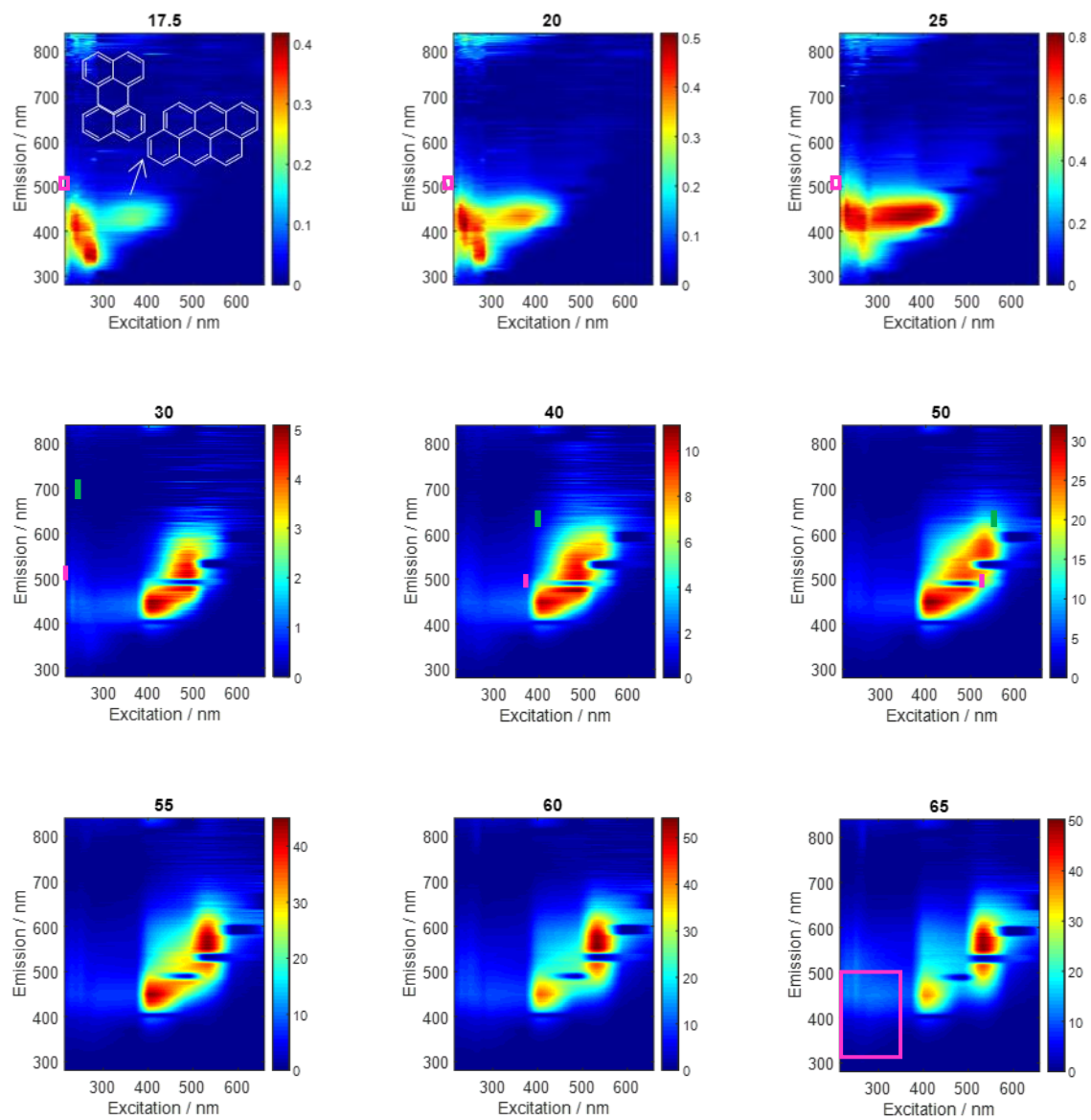
Compared to LIF spectra, the EEMs allow a better separation of the spectral contributions of PAHs and thus a more accurate identification of the chromophores. However, the separation of the different contributions of PAHs in the flames remains challenging. Although not implemented here, [the use of specific methods allowing the accurate analytical treatments of the images such as chemometric methods \[62,63\]](#) would probably improve this separation. However, such analysis would also require proper knowledge of the complete set of the individual EEM of the target PAHs, which was not achievable here. This being said, as discussed below the qualitative information conveyed in the EEM appears relevant for the identification of the species implicated in soot inception.

4. Results and discussion

4.1 Fluorescence EEMs obtained in the flame

The flame EEMs recorded from the fluorescence spectra measured in the flame as a function of the HAB (from 10 to 90 mm) are shown in **Figure 3**. The dark zones appearing on certain images around specific visible excitation wavelengths are due to the notch filters used to suppress the intense scattering signal at the excitation wavelength. Despite the low laser energy used for these measurements, some parasite LII (long vertical broadlines) appears upon UV excitation at the HABs where the soot volume fraction is high, i.e above 70 mm HAB. The purple, green and white rectangles drawn on the images identify spectral regions characteristic of the different types of species discussed below. The purple rectangle corresponds to the spectral region characteristic of the most intense spectral features of the 15 standard PAHs identified with the reference EEM as discussed in section 3.2. The white and green rectangles identify two additional spectral regions characterizing species of different nature than the referenced PAHs discussed below.





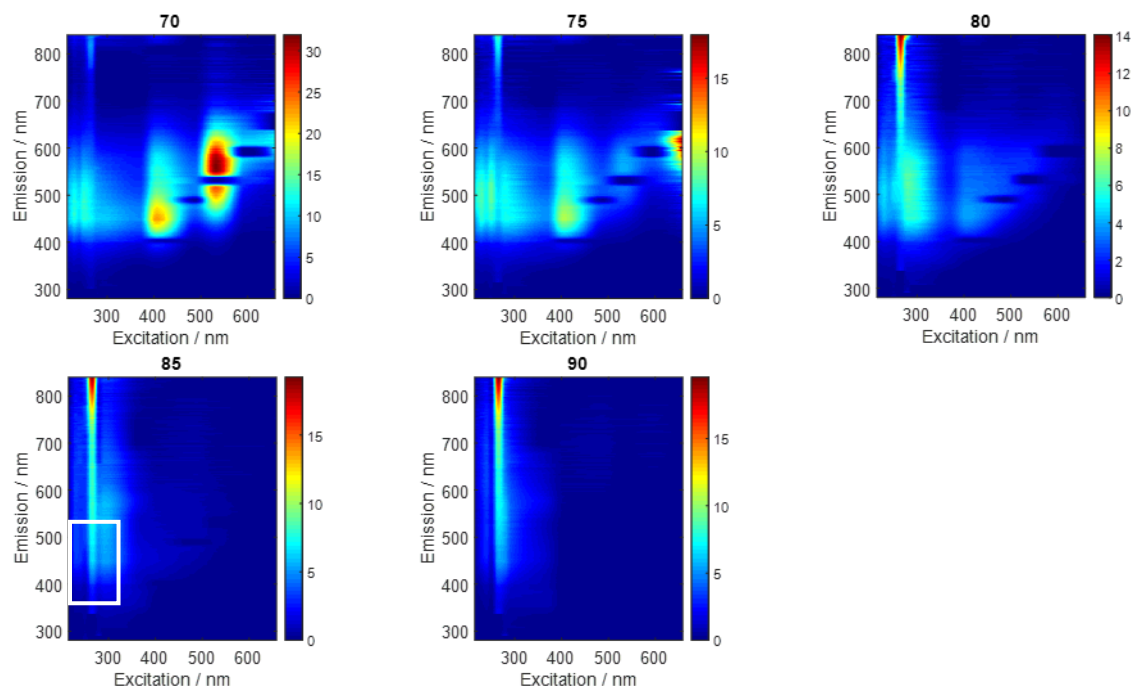


Figure 3: EEM of the methane diffusion flame as a function of the HAB from 10 to 90 mm. The emission spectra were obtained at 215, 220, 230, 240, 250, 265, 280, 290, 370, 405, 488, 532, 594, and 658 nm excitation wavelength.

4.2 Discussion on the fluorescence EEM

As can be seen in **figure 3**, the first identified spectral features in the flame EEMs is found between 200 and 350 nm in excitation and 325 and 500 nm in emission that corresponds to the spectral range characterizing the main intense bands of the reference PAHs. This spectral feature, delimited by the purple rectangle, is prominent in the flame EEMs between 10 and 25 mm HAB [37]. From the comparison with the reference EEMs, at 10 mm HAB the contribution of naphthalene can be clearly identified. At 12.5 mm HAB, additional contributions appear that are characteristic of the formation of larger PAHs with up to 3 aromatic rings such as phenanthrene and anthracene. At 15 mm HAB, the contribution of larger PAHs (up to 4 aromatic rings) as pyrene and fluoranthene can be distinguished, characterized in particular by the appearance of broad spectral structures around 400 nm in emission. The flame EEMs at 17.5 mm and 20 mm

HAB show the contributions of PAHs with up to 5 and 6 aromatic rings such as benzo[a]pyrene, perylene and anthanthrene. Above 25 mm HAB, the spectral components characteristic of 2 and 3 aromatic rings PAHs progressively decrease when compared to the spectral components of 4, 5 and 6 aromatic rings PAHs.

However, the intense fluorescence signal that emerges in the visible region above 400 nm in both excitation and emission cannot be reproduced by any combinations of the reference EEMs of PAHs. This second spectral feature, delimited by the green rectangle in **figure 3**, dominates the flame EEM between 30 and 70 mm HAB, reaching its maximum around 55-60 mm HAB. As reported in **figure 4**, this visible fluorescence signal can be roughly structured into three zones. The intensity of the profiles in **figure 4** is calculated as the sum of the intensity of the EEM_{ij} signal of each zone.

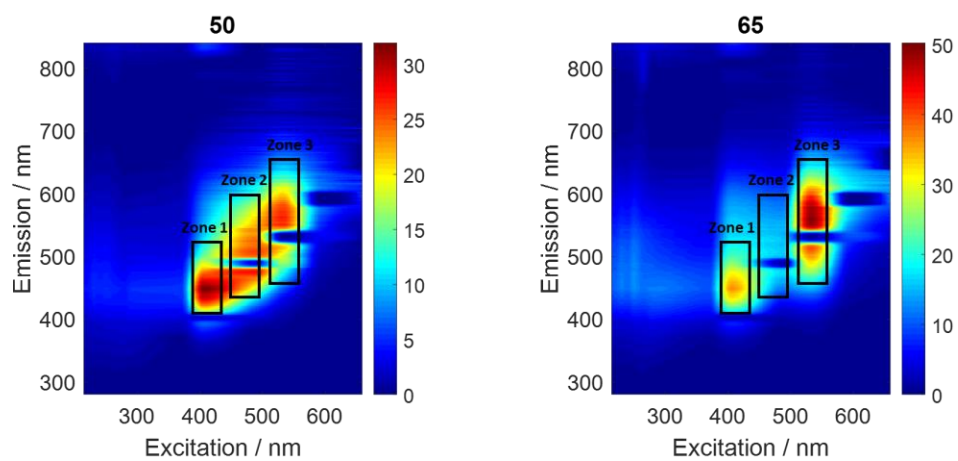
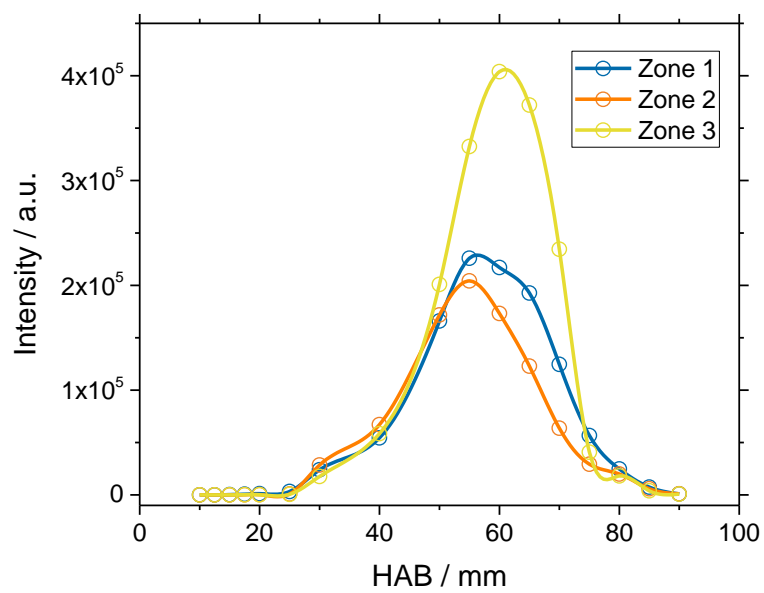
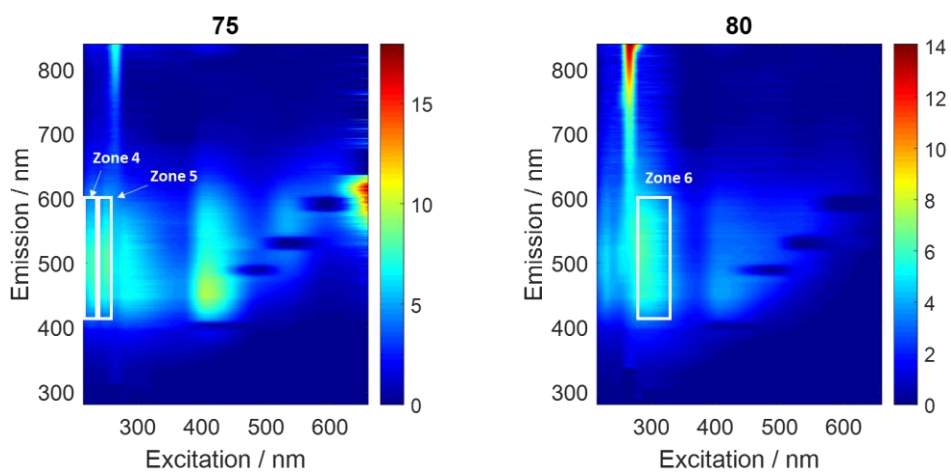


Figure 4: Evolution of the intensity of the three spectral zones in the visible as a function of the HAB.

The fluorescence signal defined by the zone 1 might be affected by weak spectral overlap with visible fluorescence signals emitted by large PAHs. However, the fluorescence signals observed at higher excitation wavelengths (488 nm, 532 nm, 594 nm, and 658 nm) in zone 2 and zone 3 clearly show the involvement of species different from neutral PAH monomers. It is to be noted that the UV signals characteristic of the PAH contributions are still present in the flame EEMs at these HABs, but its visualization is overwhelmed by the stronger intensity of the visible signal. Finally, this visible fluorescence signal abruptly disappears above 70 mm HAB, i.e. in a region slightly after the first LII signals characterizing the soot particles can be detected in this flame [37]. This suggests that the species at the origin of these fluorescence visible signals might be related to soot inception process.

Above 75 mm HAB, the second spectral feature disappear. In parallel, an additional third spectral feature appears corresponding to broadband fluorescence emission (400-600 nm) under UV excitation that is delimited by the white rectangle in **figure 3**. Three main contributions can be distinguished as shown in **figure 5**, centered respectively at 225, 245 and 300 nm in excitation (zones 4, 5 and 6, respectively). These structures correspond to fluorescent species appearing in the rising edge of the LII profile (reported **figure 6**) and disappearing around 90 mm in the mature soot region. In a previous work, we suggested that these signals might characterize the formation of van der Waals dimers of PAHs stabilized by covalent C-C bonds by comparison with simulated spectra based on a simple spectroscopic model [39] and further supported by chemical analysis made by time-of-flight secondary ion mass spectrometry (ToF-SIMS) [64]. Recently, Bartos et al. [22] related such signals in similar sooting flames to clusters of PAHs according to time-resolved LIF measurements done with picosecond laser. Theoretical research

carried out by Krueger et al. [26,65] showcases that numerous noncovalent and aliphatically-bridged complexes, namely PAH excimers, formed from PAHs of size relevant to flames, can exhibit fluorescence emission within the visible spectrum upon UV excitation. They notably specified in this work that, as the formation of PAH excimers (“excited dimers”) resulted from the laser excitation of only one of the monomers constituting the dimer, the absorption spectra of dimers was not affected by the structure of the aromatic complex which may therefore be excited in the UV range.



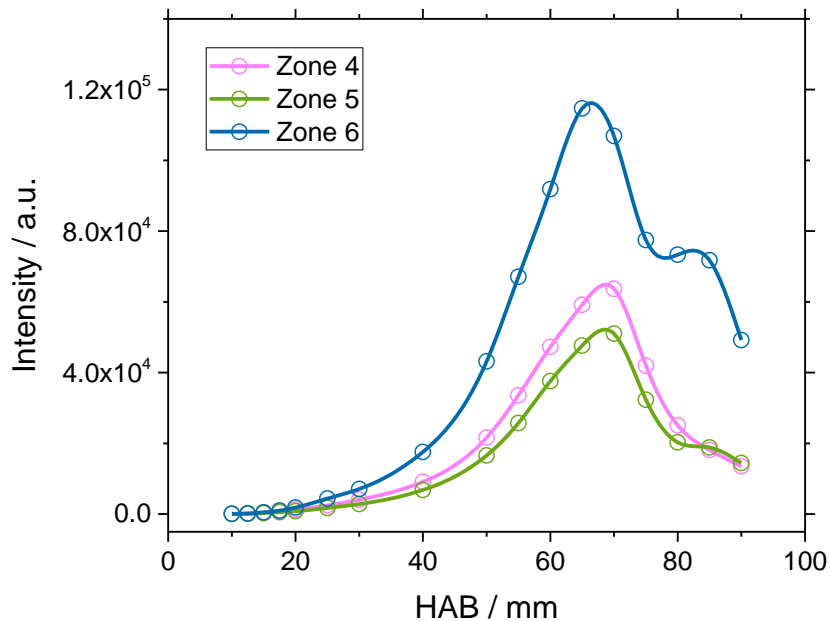


Figure 5: Evolution of the intensity of zones 4, 5 and 6 under UV excitation as a function of the HAB

The spectral features in zones 4, 5 and 6 share some properties with carbon dots (CDs). Such species have been indeed identified by different groups [7–10,66] to be formed in sooting flames. These fluorescent compounds corresponding to not completely graphitic nanosized structures (<20 nm) are characterized by high quantum yield having spectral characteristics [11] compatible with the spectral signals observed here. In particular, they present a fairly large Stokes shift (greater than 100 nm) of the fluorescence spectra with respect to the excitation wavelength and a position of the fluorescence spectrum dependent on the excitation wavelength [13,67,68]. In the literature, it appears that these properties depend on the synthesis conditions of the CD. However, the understanding of the origin and nature of the fluorescence of CDs is still incomplete. In particular, different emission mechanisms have been proposed [14]: (1) core emission, due to the conjugated π domains of the carbon core or to the quantum confinement effect [67,69]; (2) surface state emission, related to the presence of functional groups connected to the carbon backbone [70]; and (3) molecular state emission from free or bound fluorescent

molecules [71,72]. Russo et al. [73] suggested that the fluorescence of CDs taken from the flame could be due to the aromatic ring of the carbon. Other hypothesis suggested that the appearance of surface functional groups and the oxidation of the surface of these compounds could be responsible for the mechanism behind the fluorescence of CDs [68]

To sum up all these observations, the analysis of the flame EEMs reveals at least three different types of species, discernible according to their distinct photophysical behaviors upon laser excitation. The first type is characterized by excitation in the UV range 215-350 nm and fluorescence emission bands between 325-500 nm (purple rectangle in **figure 3**). This spectral signature is consistent with 2-7 aromatic rings PAHs and substituted PAHs. The second type is characterized by excitation in the visible range 400-600 nm and fluorescence emission bands at 400-650 nm (green rectangle in **figure 3**). The third type of species is characterized by excitation in the UV range 250-325 nm and fluorescence emission bands between 420-650 nm (white rectangle in **figure 3**) which appears consistent with the formation of clusters or aliphatically bridged dimers of PAHs. *The second type of species, characterized by visible emission fluorescence signal upon visible excitation wavelengths, although long described in the literature [43,46], remain the most intriguing one, and cannot be attributed to the previously identified clusters of PAHs.*

The normalized intensity profiles of the fluorescence emission of these three types of species and the previously determined LII profile [37] characterizing the soot formation along the central vertical axis of the flame have been reported in **figure 6**. We also reported in this figure the temperature profile determined elsewhere [74] and indicated the different flame regions characterizing the main steps of the soot formation providing from previous works [37–39,64].

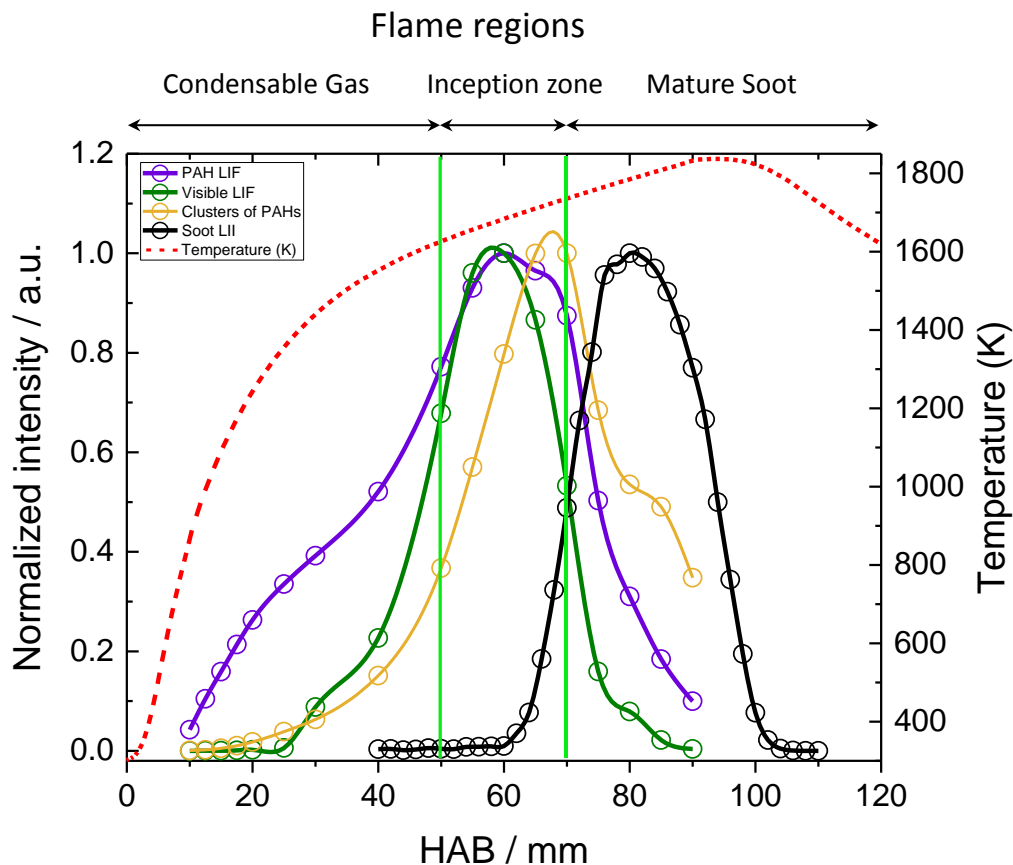


Figure 6: Normalized LIF profiles of the 3 different types of fluorescent species determined by EEM (colored solid lines) and LII profile (black solid line) reported from [39] as a function of the HAB along the central vertical axis of the flame. PAHs LIF corresponds to species of type 1, Visible LIF corresponds to species of type 2 and clusters of PAHs corresponds to species of type 3. The temperature profile (red dashed line) has been reported from [74]

These profiles highlight the successive formation of the different types of species identified along the vertical flame axis. PAHs in the gas phase (1) are detected first around 10 mm HAB, while the formation of another type of intermediate fluorophores (2) characterized by visible LIF signals begins around 30 mm. The profile of these species reaches an intensity maximum around 50-60 mm HAB, immediately before the appearance of the first measurable LII signal [37]. Then clusters of PAHs (3) still sufficiently hydrogenated to provide a fluorescence signal under UV excitation are also formed in the inception region, peaking at slightly higher HAB than species

(2), before the formation of soot particles (4). Although the exact nature of the intermediate compounds (2) and (3), mainly appearing in the soot inception zone, cannot be revealed by EEM experiments, the observed spectral structures in the visible range and their corresponding profiles strongly suggest these species to be soot precursors of different nature than 2-7 rings PAHs.

In a previous work [39], we already considered the hypothesis that the LIF signals corresponding to the species (2) and (3) might characterize the same kind of species, postulated as aliphatically bridged dimers of PAHs. This proposition was based on literature references as well as the strong similarities of the fluorescence spectral structures and lifetimes of the emission signal collected under both UV and visible excitation wavelengths. However, this previous hypothesis was made with reservations due to the lack of experimental evidence of absorption bands of dimers of PAHs in the visible range reported in the literature [39]. Based on these new results and the analysis of the EEM, we can now state that the aromatic species exhibiting visible fluorescence signal under UV excitation are clearly distinct species from the aromatic compounds fluorescing in the visible range upon visible excitation wavelength. Furthermore, as already discussed above, it is important to remind that these two kinds of species (2) and (3) are both distinct from usual PAHs (1) and soot particles (4).

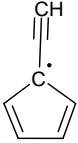
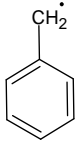
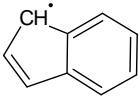
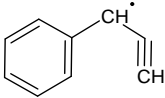
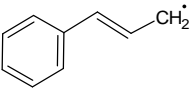
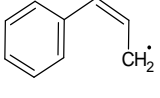
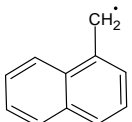
4.3 Attempt of identification of the species at the origin of the visible fluorescence

In a recent work [37], we highlighted the correlation between the intensity of the visible fluorescence measured at 532 nm in this flame [39] and the spin concentration determined by pulsed EPR characterizing the presence of resonance stabilized π -radicals (RSR). The existence of this correlation supports the hypothesis of a relationship between the visible LIF signals and the formation of RSR in sooting flames. RSR are suggested from several recent publications to be involved as key species in the inception of soot particles in flames [28,29,32,36]. In that

context, Commodo et al. [30] notably confirmed by AFM the presence of RSR PAHs in a sooting flame and provided some details on their molecular structure revealing “a large variety of molecular compounds, ranging from small aliphatic chains/substituted benzene molecules to few very large polyaromatic compounds containing up to 52 carbon atoms”. Martin et al. [35] used part of these data to show, through DFT calculations and Mulliken spin populations, that RSR PAHs might form thermally stable single bond (for strongly localized π -radicals) or multicenter bonds (for delocalized π -radicals) and leading to the formation of bridged PAHs.

Although the spectroscopy of aromatic RSRs and RSR PAHs is still a subject of study, common spectroscopic features for some of these compounds are documented in the literature. Extensive theoretical and experimental investigations have notably been conducted on the benzyl radical (C_7H_7), and highlighted absorption bands around 454 nm [75]. Besides, phenylallyl-type chromophores (C_9H_9) have been shown to absorb around 520 nm [76] while phenylpropargyl-type chromophores (C_9H_7) presents a strong origin transition at 476 nm [77]. Furthermore, benzannulation, i.e. the addition of aromatic rings to these based structures, is known to cause redshifts in the absorption wavelengths. For instance, as reported by Krechkivska et al. [78], while the benzyl radical (C_7H_7) absorbs at 454 nm, the 1-naphthylmethyl radical ($C_{11}H_9$) absorbs at 580 nm and the 9-anthracenylmethyl radical ($C_{15}H_{11}$) at 727 nm. Besides, in a recent review, Schmidt highlighted that from the analysis of a large number of hydrocarbon RSR, a rule-of-thumb emerged regarding the excitation energy, stated that PAH- CH_2 radicals are likely to absorb at about 2 times the absorption wavelength of the corresponding PAH. From this work, anthracenylmethyl ($C_{14}H_9-CH_2$) and pyrenylmethyl ($C_{16}H_9-CH_2$) are thus expected to absorb in the visible range around 500 nm.

Based on the available data in the literature, we established in **table 1** a list of some potential aromatic RSR expected to form in sooting flames and presenting absorption transitions in the visible range. This list of RSR proposes some possible candidates matching the visible absorption range of the spectral structures observed in the flame EEM. Interestingly, some of these RSR, considered as soot precursors, have molecular weights and structures matching the sampled species determined from sooting flames and discussed just above.

RSR	Formulae	m/z	Structure	Origin absorption band (nm)
fulvenallenyl	C ₇ H ₅	89		401 [79]
benzyl	C ₇ H ₇	91		454 [75]
indenyl	C ₉ H ₇	115		415 [80]
phenylpropargyl	C ₉ H ₇	115		476 [77]
trans-1-phenylallyl	C ₉ H ₉	117		521 [76]
cis-1-phenylallyl	C ₉ H ₉	117		528 [76]
1-naphthylmethyl	C ₁₁ H ₉	141		580 [75]

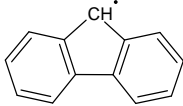
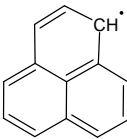
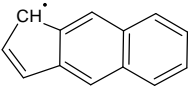
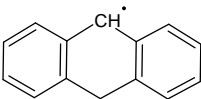
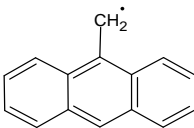
Fluorenyl	$C_{13}H_9$	165		490 [81]
Phenalenyl	$C_{13}H_9$	165		546 [82]
Benz[f]indenyl	$C_{13}H_9$	165		510 [81]
9-hydroanthracenyl	$C_{14}H_{11}$	179		520 [78]
9-anthracenylmethyl	$C_{15}H_{11}$	191		727 [83]

Table 1: Examples of aromatic RSRs known to present absorption bands in the visible range

However, while the absorption spectral features of these compounds are correctly documented in the literature, characterized by well-defined electronic transitions in the visible range, only a limited number of publications relate information about their fluorescence emission bands. For instance, indenyl (C_9H_7), which presents an origin absorption band around 415 nm, has never been studied by LIF in the gas phase [but only in low temperature matrix](#) [80]. It was hypothesized that the lifetime of the first excited states of this species is too short for being observed by LIF. In contrast, Reilly et al. [84] demonstrated that its isomer 1-phenylpropargyl (C_9H_7), was characterized by absorption lines at 476, 459.4, 456.2, and 455.2 nm and strong emission bands in the visible range around 476 and 503 nm. Similarly, Chalyavi et al. [75] published an extensive spectroscopic study of 1-naphthylmethyl ($C_{11}H_9$), 2-naphthylmethyl ($C_{11}H_9$), and α -acenaphthenyl ($C_{12}H_9$). In this work, they highlighted that all these species

exhibited absorption and emission bands around 580 nm. These data, although limited to a few RSRs of low mass PAHs, highlight the possibilities of absorption and emission of such compounds in the visible range matching the spectral structures observed in the flame EEM reported in **figure 7**, which might in this case result from the cumulative contribution of π -chromophores of several RSR PAHs as reported in **table 1**.

The hypothesis appears also consistent with the evolution of the EEM in the proximity of the inception zone as reported in **figure 7**. We magnified here the visible structure for a better appreciation of the evolution of the spectral structure with HAB. We also reported below the images the typical shape of the PAH absorption features and the position of the origin bands of a few aromatic RSR. As can be seen on the images, the global visible structure slightly enlarges with HAB until 50-55 mm HAB (maximum intensity) and then decrease both in size and intensity up to 75 mm HAB. The very broad spectral feature of this fluorescent structure suggests the implication of several π -chromophores, potentially including RSR PAHs as reported under the images, which might be formed by H addition or H abstraction from neutral PAHs. The increase of the intensity of the whole structure up to 55 mm HAB might characterize the implication of different RSR which may participate to the building of the core of incipient soot [28,29,36]. The degradation then, of part of the image, would characterize the consumption and/or deactivation of these RSR species, which appears correlated with the appearance of the first LII signal characterizing the formation of soot particles around 60 mm HAB. From these data alone, it cannot be stated if the identified species are condensable species participating to the inception step or condensed species accumulating into the core of the soot nuclei.

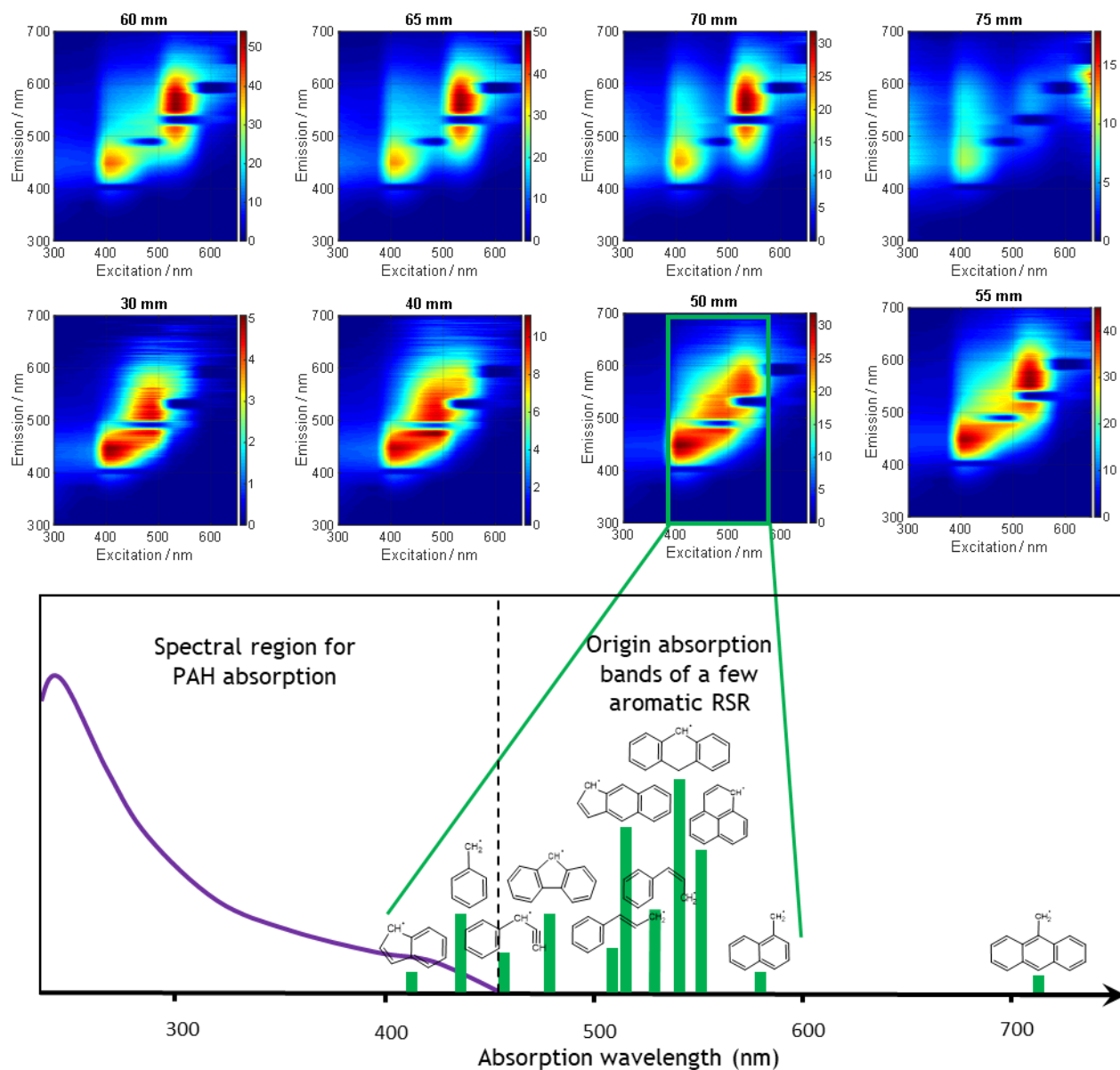


Figure 7: Evolution of the visible structures determined by the EEM fluorescence spectra in the neighborhood of the inception along the central vertical axis of the flame. Typical PAH absorption bands (purple line). The green vertical lines correspond to the origin absorption bands of several aromatic RSR (table 1).

To further support the analysis of these data, we reported in **figure 8** the intensity of the visible fluorescence signal summed over the whole spectral structure, against HAB in comparison with the concentration profile of the persistent π -radical species determined from previous EPR

experiments in this flame [37]. As can be seen, these two sets of data are characterized by very close profiles (same rise) both peaking around 60 mm HAB. The strong correlation between these two sets of data might support the hypothesis that the visible LIF signal could be a spectral signature representative of the formation of RSR PAHS in flames.

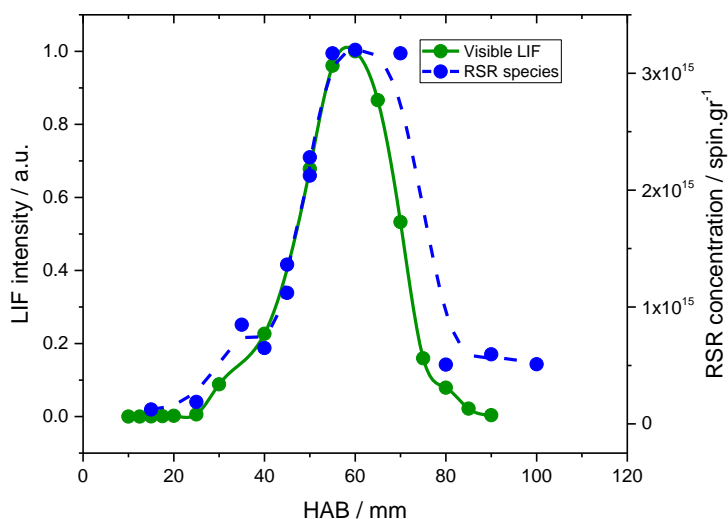


Figure 8: Normalized LIF profile (solid green line) and spin concentration of the persistent radicals detected in the samples by EPR (dashed blue line)[37] as a function of HAB in the flame.

5. Theoretical analysis: hypothesis of resonance stabilized radicals of PAHs

In order to assess the possible implication of RSR PAHs in the observed visible fluorescence signal in the EEM spectra, theoretical calculation of the spectral features of PAHs, dimers of PAHs and radical PAHs were additionally carried out.

5.1 Computational details

All the time-independent and time-dependent density functional theory (DFT and TD-DFT) calculations were performed using the Gaussian 16 software [85] with the CAM-B3LYP (long-range-corrected) Rydberg functional [86], the 6-31++G(d) basis-set [87–90], as well as the

empirical dispersion correction D3 [91]. In order to check the geometry optimizations (in the ground and excited states) of the studied molecular systems, the absence of imaginary frequencies was verified. The electronic absorption spectra were obtained by the computation of 40 excited states from the optimized ground-state geometry, the further inclusion of states having no influence on the low-lying state energies. Finally, the emission spectra were obtained by the computation of the lowest energy electronic transition from the optimized excited-state geometries.

5.2 PAHs and PAH dimers modeling

In order to better characterize the species potentially at the origin of the second spectral feature of the EEM, we first carried out a theoretical work aiming to calculate the absorption features of PAHs dimers. Two specific PAHs, namely pyrene and fluoranthene were used as reference species. To quantify the effect of the dimerization on the excitation energy of PAHs, we optimized the geometry of pyrene and fluoranthene homodimers stabilized by van der Waals interactions (vdW homo dimers) and compared their electronic transitions to that of the corresponding monomers. The results are shown at the top of Figure 9.

As expected, a red-shift upon dimerization is observed. This effect, presumably a consequence of an increased electron delocalization, is rather small (around 0.2 eV) and far from the experimental shift observed when increasing the HAB. Indeed, upon dimerization, the lowest energy transitions are red-shifted by 22 and 7 nm (-0.26 and -0.07 eV) for [pyrene](#) and [fluoranthene](#), respectively.

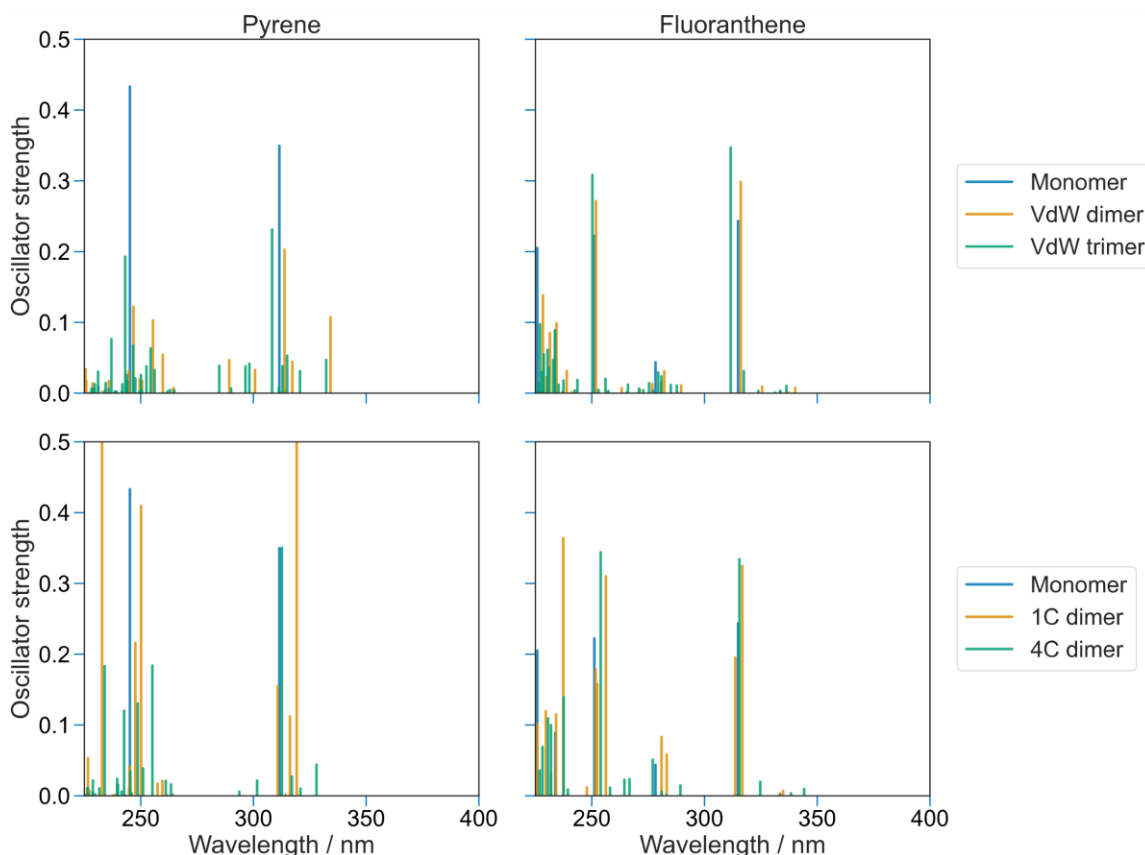


Figure 9: Low-lying electronic transitions of [pyrene](#) and [fluoranthene](#) monomers (blue) compared to their homo-dimers (orange, top), homo-trimers (green, top), 1C dimers (orange, bottom) and 4C dimers (green, bottom)

Although too weak to explain the observed visible absorption band, the calculated red-shift upon dimerization is yet interesting and one could expect that the formation of trimers or larger aliphatically bridged dimers might enhance this effect. To verify this hypothesis, we calculated and depicted the electronic transitions of the pyrene and fluoranthene vdW homotrimers at the top of Figure 9. The computed differences of -2 and -4 nm (+0.02 and +0.04 eV), which are negligible blue shifts relative to the corresponding homodimers, show that this structural change does not appreciably impact the excitation energies. On the basis of these calculations, the hypothesis of vdW oligomers to explain the visible absorption band at the origin of the visible

broad fluorescence band appears finally unlikely. The influence of additional PAHs to form oligomers is not expected to significantly change the computed values.

As suggested in our previous work [39], soot inception could be explained by the formation of dimers chemically bonded through aliphatic bridges. At the bottom of Figure 9 are depicted the electronic transitions of dimers of **pyrene** and **fluoranthene** bonded through 1C and 4C aliphatic chains. All the possible bonding schemes were computed but no significant effect on the transitions due to the position of the aliphatic chain was observed. Thus, we report herein only the results dealing with dimers bonded by their carbon atoms 2 from the nomenclature given on Figure 10.

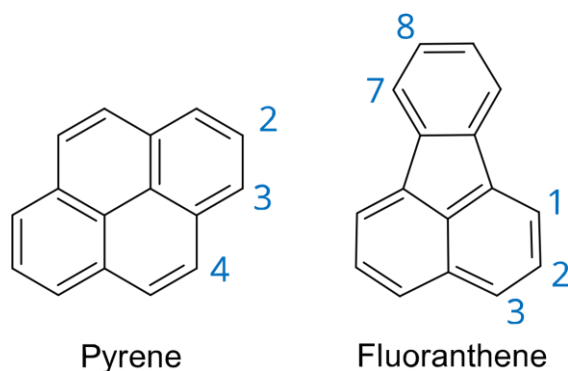


Figure 10: **Pyrene** and **fluoranthene** with the carbon atom labelling used in this work

Switching from a vdW dimer to a covalently bonded dimer modifies the longest absorption wavelengths by -15 and -6 nm (+0.17 and +0.07 eV, for 1C and 4C) for **pyrene** and by -5 and +4 nm (+0.06 and -0.04 eV, for 1C and 4C) for **fluoranthene** which do not provide a better fit to the experimental data, making this hypothesis also unlikely. These calculation confirm that dimers of PAHs can only be excited in the UV range, at excitation wavelengths close to the monomer excitation wavelengths [26,65].

5.3 PAH and PAH dimer radicals

Then, the excitation of radical PAH-based species was explored. Our calculations highlight that aromatic hydrogen abstraction of pericondensed PAHs leading to σ -radical does not induce significant changes in the electronic absorption spectrum. So, we focused on the effect of π -radical species formation where lateral chains are involved. The effect on the absorption spectrum of hydrogen abstraction of substituted PAHs was tested on [1-methylpyrene \(MePyrene\)](#) and [1-methylfluoranthene \(MeFluoranthene\)](#). To explore the effect on the dimerization of such species, we calculated the electronic transitions of a dimer formed by a methylated monomer and a regular monomer ([MePyrene-Pyrene](#), [MeFluoranthene-Fluoranthene](#) and [Me•Pyrene-Pyrene](#), [Me•Fluoranthene-Fluoranthene](#)). Finally, π -radicals were also obtained by the removal of a hydrogen atom in the aliphatic bridge connecting two monomers (4C•) which should have a similar effect as the one computed for [Me•Pyrene-Pyrene](#) and [Me•Fluoranthene-Fluoranthene](#) dimers. The results are shown in Figure 11.

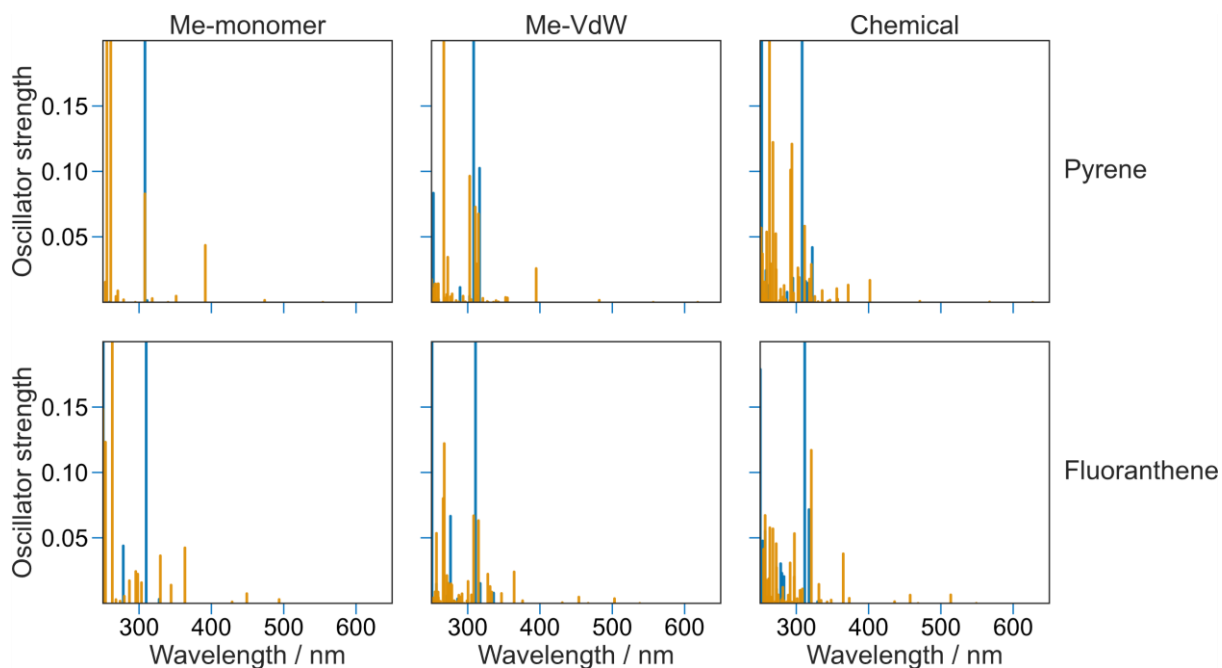


Figure 11: Electronic transitions of methylated monomer, methylated vdW dimers and chemical dimers of [pyrene](#) and [fluoranthene](#) in their non-radical (blue) and radical (orange) form. The y-axes were zoomed to better see the radical's transitions

First, by comparing the transitions of methylated and unsubstituted monomers (Figure 11, blue transitions), the methylation does not seem to have a significant effect on the absorption spectrum with shifts of 3 and 1 nm (-0.03 and -0.01 eV) for [MePyrene](#) and [MeFluoranthene](#), respectively. This observation can also be made for the methylated vdW dimers *vs.* the non-methylated ones.

While comparing the electronic transitions of radical species, we note that hydrogen-abstraction to form a π -radical always yields large transition energy shifts on the spectrum, along with a drastic reduction of the oscillator strength. Non-zero oscillator strengths are still observed for transitions in the 500-600 nm range, which suggests the possibility to excite such species. The shifts when switching from the non-radical to the radical species are listed in **Table 2**.

	Wavelength / nm (eV)		
	Me•monomer	Me•vdW	4C•
Pyrene	243 (-1.75)	302 (-1.91)	305 (-1.87)
Fluoranthene	166 (-1.27)	202 (-1.39)	218 (-1.49)

Table 2: Red-shift of the longest excitation wavelength when switching from the non-radical Me-Monomer, Me-vdW, and chemical species, to their radical counter-part.

Me•vdW and 4C• species have similar absorption spectra, which illustrates that the electronic properties of these two systems are similar. The red-shifts are large and closer to those observed experimentally. Thus, the formation of a π -radical in an aliphatic chain at the edge of a peri-condensed PAH is able to drastically red-shift the absorption wavelength.

5.4 Fluorescence computation

For further evidences on the origin of the fluorescence signal, we optimized pyrene, [MePyrene](#) and [Me•Pyrene](#) in their lowest electronic excited-state and computed their fluorescence emission properties. The methylation of Pyrene does not induce any significant change in the fluorescence spectra (computed emission maxima at 332 and 330 nm for [MePyrene](#) and [pyrene](#), respectively, consistent with the close resemblance between pyrene and [MePyrene](#) experimental emission spectra [92]).

The abstraction of a hydrogen atom from the methyl group of [MePyrene](#) to yield [Me•Pyrene](#) induces a bathochromic effect of 370 nm (-1.97 eV), moving the emission maximum to 702 nm. The oscillator strength associated to this transition (computed for the absorption phenomenon) is $f=0.0000$. However, numerous effects influence the emission of a species beyond f value.

Hence, this null value does not necessarily mean that the transition is forbidden, but it could be observed due to vibronic coupling as in the case of Pyrene [93] (which yields a comparable oscillator strength value of 0.0006). This observation could be attributed, as stated by Krueger et al. [26], to the fact that at flame temperature, both intra- and intermolecular dimer modes are excited, leading to non-zero oscillator strengths. The involvement of the carbon bearing the single electron in the lowest energy transition (**figure 12**) is, as expected, larger in the case of [MePyrene](#), confirming the important role of the radical.

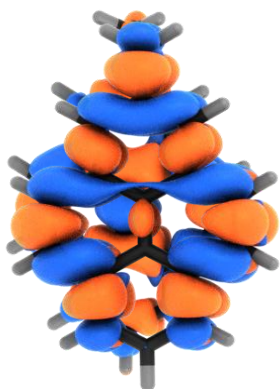


Figure 12: Variation of the electron density during the lowest energy transition in [MePyrene](#) (left) and [Me•Pyrene](#) (right). The blue and orange colors indicate density decrease and increase, respectively

This spectral analysis therefore supports the assignment of the fluorescence signal to π -radicals, rather than σ radicals, as well as to bridged aromatics RSR structures linked by aliphatic chains to explain the visible fluorescence signal. However, the strong intensity of the experimentally observed visible fluorescence emission signals cannot find for now satisfactory explanation with these calculations. Especially the oscillator strengths both in absorption and emission of the calculated RSR PAH structures are too low with the current model to explain the observed signals. Several factors might bias this comparison. First, the strong difference of temperature between the calculated (0 K) and the measured spectra (~ 1700 K). It is well known that temperature can strongly impact the electronic transitions by allowing the excitation of energetic levels not populated at low temperature. The strong intensity of the measured signal might also be related to the accumulation of the RSR species inside the core of the soot particles leading to a

substantial increase of the fluorescence signal. And finally, issues can also provide from the model itself, as the optimization of a radical dimer in its excited-state is challenging, due to the spreading of spin density on the whole systems that creates unexpected bonds between sub-systems.

6. Conclusions

This study aims to characterize the chemical species at soot inception in a laminar diffusion flame of methane. For this purpose, a dedicated laser induced fluorescence (LIF) experimental setup was implemented to determine the excitation-emission matrix (EEM) all along the vertical central axis of the flame with an adequate spatial resolution enabling to show specific evolutions of the spectral structures characterizing different types of aromatic species during the whole steps of the soot formation. In parallel to this experimental work, a theoretical study was implemented based on ab initio calculations aiming to calculate the electronic transitions of selected key aromatic species in the soot formation, included polycyclic aromatic hydrocarbons (PAHs), dimers of PAHs, PAH radicals and radical dimers.

The analysis of the EEMs showed the existence of three different spectral features specific to the inception zone of the flame and characterized by unique optical properties, only one of which could be clearly assigned to PAHs. According to our analysis, PAHs up to coronene can be identified within relatively narrow spectral region defined as 215-350 nm in excitation and 325-500 nm in emission. However, the EEMs determined in the flame unveiled the presence of additional types of fluorophore compounds within a distinct spectral range in 250-325 nm in excitation and 420-650 nm in emission, consistent with the calculated optical properties of (aliphatically) bridged dimers of PAHs. Finally, the EEMs highlighted a third spectral feature characterized by fluorescence signals within a visible spectral range in 400-600 nm excitation

and 400-650 nm emission. The analysis of these last spectral structure showed similitudes with the spectral properties of several aromatic resonance-stabilized radicals (RSR). This hypothesis is further supported by the correlation observed between the profile of the intensity of the visible fluorescence and the spin concentration profile of persistent radicals determined previously by electron paramagnetic resonance in this flame.

Theoretical calculation of a few specific PAHs, dimers of PAHs and RSR PAHs presented in this work allowed to deepen and support this analysis. These calculations reveal indeed that the spectroscopic properties PAHs as well as dimers of PAHs, either chemical or VdW dimers, cannot explain the visible absorption bands at the origin of the visible broad fluorescence bands observed in the EEM spectra. Conversely, theoretical calculations for RSR PAHS highlight electronic transitions in the visible range and the possibilities of fluorescence of such kind of compounds coherent with the observed visible spectral structures in the EEM. This analysis hence suggests that the visible broad fluorescence bands might be indicative of the formation of resonantly stabilized π -radicals in sooting flames. However, although spectrally consistent, the strong intensity of the measured signal could not be satisfactorily explained by the ab initio model. Potential issues due to the temperature, accumulation of the species in condensed materials (core of the soot) or improvement of the model itself have been suggested to explain these inconstancies. We hope that ongoing computations might bring complementary information regarding the analysis of these spectra, notably by extending the study to other radicals like aromatic dimers of RSR and biradicals, though optimizing the excited-state of radical dimers is challenging due to spin density spreading and unexpected bonds formation.

Acknowledgments

This work was supported by the Agence Nationale de la Recherche through the LABEX CAPP (ANR-11-LABX-0005), the Agence de l'Environnement et De la Maîtrise de l'Energie ADEME, the Ministry of Higher Education and Research, Hauts de France Regional Council and European Regional Development Fund (ERDF) through the Contrat de Projets Etat Region (CPER CLIMIBIO). We thank the CRI (Centre de Ressources Informatiques) of the University of Lille for providing computation time for part of the calculations. The authors finally thank the Centre d'Etudes et de Recherches Lasers et Applications CERLA for technical help and financial support to this project.

References

- [1] I.M. Kennedy, The health effects of combustion-generated aerosols, *Proceedings of the Combustion Institute* 31 (2007) 2757–2770. <https://doi.org/10.1016/j.proci.2006.08.116>.
- [2] G. Oberdörster, Z. Sharp, V. Atudorei, A. Elder, R. Gelein, W. Kreyling, C. Cox, Translocation of Inhaled Ultrafine Particles to the Brain, *Inhalation Toxicology* 16 (2004) 437–445. <https://doi.org/10.1080/08958370490439597>.
- [3] K.-H. Kim, S.A. Jahan, E. Kabir, R.J.C. Brown, A review of airborne polycyclic aromatic hydrocarbons (PAHs) and their human health effects, *Environment International* 60 (2013) 71–80. <https://doi.org/10.1016/j.envint.2013.07.019>.
- [4] J.B. Howard, J.P. Longwell, J.A. Marr, C.J. Pope, W.F. Busby, A.L. Lafleur, K. Taghizadeh, Effects of PAH isomerizations on mutagenicity of combustion products, *Combustion and Flame* 101 (1995) 262–270. [https://doi.org/10.1016/0010-2180\(94\)00210-J](https://doi.org/10.1016/0010-2180(94)00210-J).
- [5] T.C. Bond, S.J. Doherty, D.W. Fahey, P.M. Forster, T. Berntsen, B.J. DeAngelo, M.G. Flanner, S. Ghan, B. Kärcher, D. Koch, S. Kinne, Y. Kondo, P.K. Quinn, M.C. Sarofim, M.G. Schultz, M. Schulz, C. Venkataraman, H. Zhang, S. Zhang, N. Bellouin, S.K. Guttikunda, P.K. Hopke, M.Z. Jacobson, J.W. Kaiser, Z. Klimont, U. Lohmann, J.P. Schwarz, D. Shindell, T. Storelvmo, S.G. Warren, C.S. Zender, Bounding the role of black carbon in the climate system: A scientific assessment, *Journal of Geophysical Research: Atmospheres* 118 (2013) 5380–5552. <https://doi.org/10.1002/jgrd.50171>.
- [6] R.F. Service, Study Fingers Soot as a Major Player in Global Warming, *Science* 319 (2008) 1745–1745. <https://doi.org/10.1126/science.319.5871.1745>.
- [7] A. Rahy, C. Zhou, J. Zheng, S.Y. Park, M.J. Kim, I. Jang, S.J. Cho, D.J. Yang, Photoluminescent carbon nanoparticles produced by confined combustion of aromatic compounds, *Carbon* 50 (2012) 1298–1302. <https://doi.org/10.1016/j.carbon.2011.10.052>.

- [8] C. Russo, B. Apicella, A. La Rocca, M. Sirignano, Fluorescent carbon dots synthesis in premixed flames: Influence of the equivalence ratio, *Carbon* 201 (2023) 659–666. <https://doi.org/10.1016/j.carbon.2022.09.061>.
- [9] O. Kozák, M. Sudolská, G. Pramanik, P. Cígler, M. Otyepka, R. Zbořil, Photoluminescent Carbon Nanostructures, *Chem. Mater.* 28 (2016) 4085–4128. <https://doi.org/10.1021/acs.chemmater.6b01372>.
- [10] M. Fu, F. Ehrat, Y. Wang, K.Z. Milowska, C. Reckmeier, A.L. Rogach, J.K. Stolarczyk, A.S. Urban, J. Feldmann, Carbon Dots: A Unique Fluorescent Cocktail of Polycyclic Aromatic Hydrocarbons, *Nano Lett.* 15 (2015) 6030–6035. <https://doi.org/10.1021/acs.nanolett.5b02215>.
- [11] Y.-P. Sun, B. Zhou, Y. Lin, W. Wang, K.A.S. Fernando, P. Pathak, M.J. Meziani, B.A. Harruff, X. Wang, H. Wang, P.G. Luo, H. Yang, M.E. Kose, B. Chen, L.M. Veca, S.-Y. Xie, Quantum-Sized Carbon Dots for Bright and Colorful Photoluminescence, *J. Am. Chem. Soc.* 128 (2006) 7756–7757. <https://doi.org/10.1021/ja062677d>.
- [12] H.-L. Yang, L.-F. Bai, Z.-R. Geng, H. Chen, L.-T. Xu, Y.-C. Xie, D.-J. Wang, H.-W. Gu, X.-M. Wang, Carbon quantum dots: Preparation, optical properties, and biomedical applications, *Materials Today Advances* 18 (2023) 100376. <https://doi.org/10.1016/j.mtadv.2023.100376>.
- [13] T. Yuan, T. Meng, P. He, Y. Shi, Y. Li, X. Li, L. Fan, S. Yang, Carbon quantum dots: an emerging material for optoelectronic applications, *J. Mater. Chem. C* 7 (2019) 6820–6835. <https://doi.org/10.1039/C9TC01730E>.
- [14] C.M. Carbonaro, R. Corpino, M. Salis, F. Mocci, S.V. Thakkar, C. Olla, P.C. Ricci, On the Emission Properties of Carbon Dots: Reviewing Data and Discussing Models, *C* 5 (2019) 60. <https://doi.org/10.3390/c5040060>.
- [15] M. Commodo, A. D’Anna, G. De Falco, R. Larciprete, P. Minutolo, Illuminating the earliest stages of the soot formation by photoemission and Raman spectroscopy, *Combustion and Flame* 181 (2017) 188–197. <https://doi.org/10.1016/j.combustflame.2017.03.020>.
- [16] H. Wang, Formation of nascent soot and other condensed-phase materials in flames, *Proc. Combust. Inst.* 33 (2011) 41–67. <https://doi.org/10.1016/j.proci.2010.09.009>.
- [17] N.A. Eaves, S.B. Dworkin, M.J. Thomson, The importance of reversibility in modeling soot nucleation and condensation processes, *Proceedings of the Combustion Institute* 35 (2015) 1787–1794. <https://doi.org/10.1016/j.proci.2014.05.036>.
- [18] M.R. Kholghy, G.A. Kelesidis, S.E. Pratsinis, Reactive polycyclic aromatic hydrocarbon dimerization drives soot nucleation, *Phys. Chem. Chem. Phys.* 20 (2018) 10926–10938. <https://doi.org/10.1039/C7CP07803J>.
- [19] P. Desgroux, A. Faccineto, X. Mercier, T. Mouton, D. Aubagnac Karkar, A. El Bakali, Comparative study of the soot formation process in a “nucleation” and a “sooting” low pressure premixed methane flame, *Combustion and Flame* 184 (2017) 153–166. <https://doi.org/10.1016/j.combustflame.2017.05.034>.
- [20] B.A. Adamson, S.A. Skeen, M. Ahmed, N. Hansen, Nucleation of soot: experimental assessment of the role of polycyclic aromatic hydrocarbon (PAH) dimers, *Zeitschrift Für Physikalische Chemie* 234 (2020) 1295–1310. <https://doi.org/10.1515/zpch-2020-1638>.
- [21] J.W. Martin, M. Salamanca, M. Kraft, Soot inception: Carbonaceous nanoparticle formation in flames, *Progress in Energy and Combustion Science* 88 (2022) 100956. <https://doi.org/10.1016/j.pecs.2021.100956>.

- [22] D. Bartos, M. Sirignano, M.J. Dunn, A. D'Anna, A.R. Masri, Soot inception in laminar coflow diffusion flames, *Combustion and Flame* 205 (2019) 180–192. <https://doi.org/10.1016/j.combustflame.2019.03.026>.
- [23] M. Frenklach, A.M. Mebel, On the mechanism of soot nucleation, *Phys. Chem. Chem. Phys.* 22 (2020) 5314–5331. <https://doi.org/10.1039/D0CP00116C>.
- [24] H. Sabbah, L. Biennier, S.J. Klippenstein, I.R. Sims, B.R. Rowe, Exploring the Role of PAHs in the Formation of Soot: Pyrene Dimerization, *Journal of Physical Chemistry Letters* 1 (2010) 2962–2967. <https://doi.org/10.1021/jz101033t>.
- [25] F. Schulz, M. Commodo, K. Kaiser, G. De Falco, P. Minutolo, G. Meyer, A. D'Anna, L. Gross, Insights into incipient soot formation by atomic force microscopy, *Proceedings of the Combustion Institute* 37 (2019) 885–892. <https://doi.org/10.1016/j.proci.2018.06.100>.
- [26] R.A. Krueger, G. Blanquart, Predicting aromatic exciplex fluorescence emission energies, *Phys. Chem. Chem. Phys.* 21 (2019) 10325–10335. <https://doi.org/10.1039/C9CP02027F>.
- [27] B.D. Adamson, S.A. Skeen, M. Ahmed, N. Hansen, Detection of Aliphatically Bridged Multi-Core Polycyclic Aromatic Hydrocarbons in Sooting Flames with Atmospheric-Sampling High-Resolution Tandem Mass Spectrometry, *J. Phys. Chem. A* 122 (2018) 9338–9349. <https://doi.org/10.1021/acs.jpca.8b08947>.
- [28] K.O. Johansson, M.P. Head-Gordon, P.E. Schrader, K.R. Wilson, H.A. Michelsen, Resonance-stabilized hydrocarbon-radical chain reactions may explain soot inception and growth, *Science* 361 (2018) 997–1000. <https://doi.org/10.1126/science.aat3417>.
- [29] J.W. Martin, D. Hou, A. Menon, L. Pascazio, J. Akroyd, X. You, M. Kraft, Reactivity of Polycyclic Aromatic Hydrocarbon Soot Precursors: Implications of Localized π -Radicals on Rim-Based Pentagonal Rings, *J. Phys. Chem. C* 123 (2019) 26673–26682. <https://doi.org/10.1021/acs.jpcc.9b07558>.
- [30] M. Commodo, K. Kaiser, G. De Falco, P. Minutolo, F. Schulz, A. D'Anna, L. Gross, On the early stages of soot formation: Molecular structure elucidation by high-resolution atomic force microscopy, *Combustion and Flame* 205 (2019) 154–164. <https://doi.org/10.1016/j.combustflame.2019.03.042>.
- [31] Z.D. Levey, B.A. Laws, S.P. Sundar, K. Nauta, S.H. Kable, G. da Silva, J.F. Stanton, T.W. Schmidt, PAH Growth in Flames and Space: Formation of the Phenalenyl Radical, *J. Phys. Chem. A* 126 (2022) 101–108. <https://doi.org/10.1021/acs.jpca.1c08310>.
- [32] G. Vitiello, G. De Falco, F. Picca, M. Commodo, G. D'Errico, P. Minutolo, A. D'Anna, Role of radicals in carbon clustering and soot inception: A combined EPR and Raman spectroscopic study, *Combustion and Flame* 205 (2019) 286–294. <https://doi.org/10.1016/j.combustflame.2019.04.028>.
- [33] A. Valavanidis, N. Iliopoulos, G. Gotsis, K. Fiotakis, Persistent free radicals, heavy metals and PAHs generated in particulate soot emissions and residue ash from controlled combustion of common types of plastic, *J Hazard Mater* 156 (2008) 277–284. <https://doi.org/10.1016/j.jhazmat.2007.12.019>.
- [34] A.S. Savchenkova, A.S. Semenikhin, I.V. Chechet, S.G. Matveev, M. Frenklach, A.N. Morozov, A.M. Mebel, Mechanism of E-bridge formation by various PAH molecules: A theoretical study, *Chemical Physics Letters* 799 (2022) 139637. <https://doi.org/10.1016/j.cplett.2022.139637>.
- [35] P.K. Selvakumar, J.W. Martin, M.D. Lorenzo, M. Paskevicius, C.E. Buckley, Role of π -Radical Localization on Thermally Stable Cross-Links Between Polycyclic Aromatic

- Hydrocarbons, *J. Phys. Chem. A* 127 (2023) 6945–6952. <https://doi.org/10.1021/acs.jpca.3c03769>.
- [36] M. Commodo, F. Picca, G. Vitiello, G. De Falco, P. Minutolo, A. D'Anna, Radicals in nascent soot from laminar premixed ethylene and ethylene-benzene flames by electron paramagnetic resonance spectroscopy, *Proceedings of the Combustion Institute* 38 (2021) 1487–1495. <https://doi.org/10.1016/j.proci.2020.08.024>.
- [37] J. Elias, A. Faccinetto, H. Vezin, X. Mercier, Investigation of resonance-stabilized radicals associated with soot particle inception using advanced electron paramagnetic resonance techniques, *Commun Chem* 6 (2023) 1–9. <https://doi.org/10.1038/s42004-023-00896-4>.
- [38] C. Irimiea, A. Faccinetto, X. Mercier, I.-K. Ortega, N. Nuns, E. Therssen, P. Desgroux, C. Focsa, Unveiling trends in soot nucleation and growth: When secondary ion mass spectrometry meets statistical analysis, *Carbon* 144 (2019) 815–830. <https://doi.org/10.1016/j.carbon.2018.12.015>.
- [39] X. Mercier, O. Carrivain, C. Irimiea, A. Faccinetto, E. Therssen, Dimers of polycyclic aromatic hydrocarbons: the missing pieces in the soot formation process, *Phys. Chem. Chem. Phys.* 21 (2019) 8282–8294. <https://doi.org/10.1039/C9CP00394K>.
- [40] C. Irimiea, A. Faccinetto, Y. Carpentier, I.-K. Ortega, N. Nuns, E. Therssen, P. Desgroux, C. Focsa, A comprehensive protocol for chemical analysis of flame combustion emissions by secondary ion mass spectrometry, *Rapid Communications in Mass Spectrometry* 32 (2018) 1015–1025. <https://doi.org/10.1002/rcm.8133>.
- [41] Y. Zhang, B. Xiao, Y. Li, P. Liu, R. Zhan, Z. Huang, H. Lin, LIF diagnostics for selective and quantitative measurement of PAHs in laminar premixed flames, *Combustion and Flame* 222 (2020) 5–17. <https://doi.org/10.1016/j.combustflame.2020.08.018>.
- [42] S. Bejaoui, X. Mercier, P. Desgroux, E. Therssen, Laser induced fluorescence spectroscopy of aromatic species produced in atmospheric sooting flames using UV and visible excitation wavelengths, *Combustion and Flame* 161 (2014) 2479–2491. <https://doi.org/10.1016/j.combustflame.2014.03.014>.
- [43] F. Beretta, V. Cincotti, A. D'Alessio, P. Menna, Ultraviolet and visible fluorescence in the fuel pyrolysis regions of gaseous diffusion flames, *Combustion and Flame* 61 (1985) 211–218.
- [44] Z. Chi, B.M. Cullum, D.L. Stokes, J. Mobley, G.H. Miller, M.R. Hajaligol, T. Vo-Dinh, High-temperature vapor detection of polycyclic aromatic hydrocarbon fluorescence, *Fuel* 80 (2001) 1819–1824.
- [45] M. Sirignano, A. Collina, M. Commodo, P. Minutolo, A. D'Anna, Detection of aromatic hydrocarbons and incipient particles in an opposed-flow flame of ethylene by spectral and time-resolved laser induced emission spectroscopy, *Combustion and Flame* 159 (2012) 1663–1669. <https://doi.org/10.1016/j.combustflame.2011.11.005>.
- [46] D.S. Coe, B.S. Haynes, J.I. Steinfeld, Identification of a source of argon-ion-laser excited fluorescence in sooting flames, *Combustion and Flame* 43 (1981) 211–214.
- [47] Y. Zhang, L. Wang, P. Liu, Y. Li, R. Zhan, Z. Huang, H. Lin, Measurement and extrapolation modeling of PAH laser-induced fluorescence spectra at elevated temperatures, *Appl. Phys. B* 125 (2018) 6. <https://doi.org/10.1007/s00340-018-7115-6>.
- [48] J. Wu, K.H. Song, T. Litzinger, S.-Y. Lee, R. Santoro, M. Linevsky, M. Colket, D. Liscinsky, Reduction of PAH and soot in premixed ethylene–air flames by addition of ethanol, *Combustion and Flame* 144 (2006) 675–687. <https://doi.org/10.1016/j.combustflame.2005.08.036>.

- [49] R.L. Vander Wal, K.A. Jensen, M.Y. Choi, Simultaneous laser-induced emission of soot and polycyclic aromatic hydrocarbons within a gas-jet diffusion flame, *Combustion and Flame* 109 (1997) 399–414.
- [50] D.W. Johnson, J.B. Callis, G.D. Christian, Rapid Scanning Fluorescence Spectroscopy, *Anal. Chem.* 49 (1977) 747A-757A. <https://doi.org/10.1021/ac50016a769>.
- [51] T. Aizawa, K. Imaichi, H. Kosaka, Y. Matsui, Measurement of Excitation-Emission Matrix of Shock-heated PAHs using a Multi-wavelength Laser Source, *SAE Trans.* 112 (2003) 906–915.
- [52] O. Monago-Maraña, A. Muñoz de la Peña, M. Al-Tameemi, T. Galeano-Díaz, A.D. Campiglia, Feasibility of Multidimensional Fluorescence at Low Temperature in Shpol'skii Matrices Combined with PARAFAC for the Quantitation of Polycyclic Aromatic Hydrocarbons, *International Journal of Experimental Spectroscopic Techniques* 3 (2019). <https://doi.org/10.35840/2631-505X/8522>.
- [53] D. Patra, A.K. Mishra, Excitation Emission Matrix Spectral Subtraction Fluorescence to Check Adulteration of Petrol by Kerosene, *Appl Spectrosc* 55 (2001) 338–342. <https://doi.org/10.1366/0003702011951740>.
- [54] T. Aizawa, H. Kosaka, Investigation of early soot formation process in a diesel spray flame via excitation-emission matrix using a multi-wavelength laser source, *International Journal of Engine Research* 9 (2008) 79–97. <https://doi.org/10.1243/14680874jer01407>.
- [55] F.J. Bauer, M.U.J. Degenkolb, F.J.T. Huber, S. Will, In situ characterisation of absorbing species in stationary premixed flat flames using UV–Vis absorption spectroscopy, *Appl. Phys. B* 127 (2021) 115. <https://doi.org/10.1007/s00340-021-07664-z>.
- [56] W. Karcher, R.J. Fordham, J.J. Dubois, P.G.J.M. Glaude, J. a. M. Lighthart, *Spectral atlas of polycyclic aromatic compounds Vol.1*, (1985).
- [57] W. Karcher, S. Ellison, M. Ewald, P. Garrigues, E. Gevers, J. Jacob, *Spectral atlas of polycyclic aromatic compounds Vol.2*, (1988).
- [58] S.E. Braslavsky, Glossary of terms used in photochemistry, 3rd edition (IUPAC Recommendations 2006), *Pure and Applied Chemistry* 79 (2007) 293–465. <https://doi.org/10.1351/pac200779030293>.
- [59] M. Kasha, Characterization of electronic transitions in complex molecules, *Discuss. Faraday Soc.* 9 (1950) 14–19. <https://doi.org/10.1039/DF9500900014>.
- [60] M. Orain, P. Baranger, B. Rossow, F. Grisch, Fluorescence spectroscopy of naphthalene at high temperatures and pressures: implications for fuel-concentration measurements, *Appl. Phys. B.* 102 (2011) 163–172.
- [61] C. Ledier, *Application de la LIF de molécules aromatiques au dosage de carburants fossiles et biocarburants.*, 2012.
- [62] D. Othoor, A.K. Mishra, Chemometric study of excitation-emission matrix fluorescence data: Quantitative analysis of petrol-kerosene mixtures, *Applied Spectroscopy* 62 (2008) 753–758. <https://doi.org/10.1366/000370208784909454>.
- [63] K. Huang, H.-L. Wu, T. Wang, M.-Y. Dong, X.-Q. Yan, R.-Q. Yu, Chemometrics-assisted excitation-emission matrix fluorescence spectroscopy for real-time migration monitoring of multiple polycyclic aromatic hydrocarbons from plastic products to food simulants, *Spectrochimica Acta Part A: Molecular and Biomolecular Spectroscopy* 304 (2024) 123360. <https://doi.org/10.1016/j.saa.2023.123360>.
- [64] A. Faccinetto, C. Irimiea, P. Minutolo, M. Commodo, A. D'Anna, N. Nuns, Y. Carpentier, C. Pirim, P. Desgroux, C. Focsa, X. Mercier, Evidence on the formation of dimers of

- polycyclic aromatic hydrocarbons in a laminar diffusion flame, *Commun. Chem.* 3 (2020) 1–8. <https://doi.org/10.1038/s42004-020-00357-2>.
- [65] R.A. Krueger, G. Blanquart, Predicting the photoresponse of soot nuclei: Spectroscopic characteristics of aromatic aggregates containing five-membered rings, *Combustion and Flame* 217 (2020) 85–92. <https://doi.org/10.1016/j.combustflame.2019.10.028>.
- [66] C. Russo, A. Carpentieri, A. Tregrossi, A. Ciajolo, B. Apicella, Blue, green and yellow carbon dots derived from pyrogenic carbon: Structure and fluorescence behaviour, *Carbon* (2022). <https://doi.org/10.1016/j.carbon.2022.09.062>.
- [67] K.J. Mintz, Y. Zhou, R.M. Leblanc, Recent development of carbon quantum dots regarding their optical properties, photoluminescence mechanism, and core structure, *Nanoscale* 11 (2019) 4634–4652. <https://doi.org/10.1039/C8NR10059D>.
- [68] H. Ding, S.-B. Yu, J.-S. Wei, H.-M. Xiong, Full-Color Light-Emitting Carbon Dots with a Surface-State-Controlled Luminescence Mechanism, *ACS Nano* 10 (2016) 484–491. <https://doi.org/10.1021/acsnano.5b05406>.
- [69] H.J. Yoo, B.E. Kwak, D.H. Kim, Competition of the roles of π -conjugated domain between emission center and quenching origin in the photoluminescence of carbon dots depending on the interparticle separation, *Carbon* 183 (2021) 560–570. <https://doi.org/10.1016/j.carbon.2021.07.054>.
- [70] S. Zhu, Y. Song, X. Zhao, J. Shao, J. Zhang, B. Yang, The photoluminescence mechanism in carbon dots (graphene quantum dots, carbon nanodots, and polymer dots): current state and future perspective, *Nano Res.* 8 (2015) 355–381. <https://doi.org/10.1007/s12274-014-0644-3>.
- [71] J. Schneider, C.J. Reckmeier, Y. Xiong, M. von Seckendorff, A.S. Susa, P. Kasák, A.L. Rogach, Molecular Fluorescence in Citric Acid-Based Carbon Dots, *J. Phys. Chem. C* 121 (2017) 2014–2022. <https://doi.org/10.1021/acs.jpcc.6b12519>.
- [72] W. Kasprzyk, T. Świergosz, S. Bednarz, K. Walas, N.V. Bashmakova, D. Bogdał, Luminescence phenomena of carbon dots derived from citric acid and urea – a molecular insight, *Nanoscale* 10 (2018) 13889–13894. <https://doi.org/10.1039/C8NR03602K>.
- [73] C. Russo, B. Apicella, A. Ciajolo, Blue and green luminescent carbon nanodots from controllable fuel-rich flame reactors, *Sci Rep* 9 (2019) 14566. <https://doi.org/10.1038/s41598-019-50919-1>.
- [74] J. Elias, A. Faccinetto, S. Batut, O. Carrivain, M. Sirignano, A. D’Anna, X. Mercier, Thermocouple-based thermometry for laminar sooting flames: Implementation of a fast and simple methodology, *International Journal of Thermal Sciences* 184 (2023) 107973. <https://doi.org/10.1016/j.ijthermalsci.2022.107973>.
- [75] N. Chalyavi, T.P. Troy, M. Nakajima, B.A. Gibson, K. Nauta, R.G. Sharp, S.H. Kable, T.W. Schmidt, Excitation and Emission Spectra of Jet-Cooled Naphthylmethyl Radicals, *J. Phys. Chem. A* 115 (2011) 7959–7965. <https://doi.org/10.1021/jp203638h>.
- [76] T.P. Troy, N. Chalyavi, A.S. Menon, G.D. O’Connor, B. Fückel, K. Nauta, L. Radom, T.W. Schmidt, The spectroscopy and thermochemistry of phenylallyl radical chromophores, *Chem. Sci.* 2 (2011) 1755–1765. <https://doi.org/10.1039/C1SC00247C>.
- [77] T.W. Schmidt, The electronic spectroscopy of resonance-stabilised hydrocarbon radicals, *International Reviews in Physical Chemistry* 35 (2016) 209–242. <https://doi.org/10.1080/0144235X.2016.1166830>.

- [78] O. Krechkivska, C.M. Wilcox, K. Nauta, S.H. Kable, T.W. Schmidt, Quantum-Induced Symmetry Breaking in the Deuterated Dihydroanthracenyl Radical, *J. Phys. Chem. A* 123 (2019) 6711–6719. <https://doi.org/10.1021/acs.jpca.9b04561>.
- [79] A. Chakraborty, J. Fulara, J.P. Maier, The Electronic Spectrum of the Fulvenallenyl Radical, *Angew. Chem.* 128 (2015) 236–239.
- [80] T. Izumida, K. Inoue, S. Noda, H. Yoshida, Electronic Spectra of Some Aromatic Free Radicals, *BCSJ* 54 (1981) 2517–2518. <https://doi.org/10.1246/bcsj.54.2517>.
- [81] J. Fulara, A. Chakraborty, J.P. Maier, Electronic Characterization of Reaction Intermediates: The Fluorenylium, Phenalenylium, and Benz[f]indenyl Cations and Their Radicals, *Angewandte Chemie International Edition* 55 (2016) 3424–3427. <https://doi.org/10.1002/anie.201511230>.
- [82] G.D. O'Connor, T.P. Troy, D.A. Roberts, N. Chalyavi, B. Fückel, M.J. Crossley, K. Nauta, J.F. Stanton, T.W. Schmidt, Spectroscopy of the Free Phenalenyl Radical, *J. Am. Chem. Soc.* 133 (2011) 14554–14557. <https://doi.org/10.1021/ja206322n>.
- [83] G.D. O'Connor, G.B. Bacskay, G.V.G. Woodhouse, T.P. Troy, K. Nauta, T.W. Schmidt, Excitation Spectra of Large Jet-Cooled Polycyclic Aromatic Hydrocarbon Radicals: 9-Anthracenylmethyl (C₁₅H₁₁) and 1-Pyrenylmethyl (C₁₇H₁₁), *J. Phys. Chem. A* 117 (2013) 13899–13907. <https://doi.org/10.1021/jp4088833>.
- [84] N.J. Reilly, D.L. Kokkin, M. Nakajima, K. Nauta, S.H. Kable, T.W. Schmidt, Spectroscopic Observation of the Resonance-Stabilized 1-Phenylpropargyl Radical, *J. Am. Chem. Soc.* 130 (2008) 3137–3142. <https://doi.org/10.1021/ja078342t>.
- [85] M.J. Frisch, G.W. Trucks, H.B. Schegel, Gaussian 16, Revision A.03, Gaussian, Inc., Wallingford CT, (2016).
- [86] T. Yanai, D.P. Tew, N.C. Handy, A new hybrid exchange–correlation functional using the Coulomb-attenuating method (CAM-B3LYP), *Chemical Physics Letters* 393 (2004) 51–57. <https://doi.org/10.1016/j.cplett.2004.06.011>.
- [87] R. Krishnan, J.S. Binkley, R. Seeger, J.A. Pople, Self-consistent molecular orbital methods. XX. A basis set for correlated wave functions, *The Journal of Chemical Physics* 72 (2008) 650–654. <https://doi.org/10.1063/1.438955>.
- [88] A.D. McLean, G.S. Chandler, Contracted Gaussian basis sets for molecular calculations. I. Second row atoms, Z=11–18, *The Journal of Chemical Physics* 72 (2008) 5639–5648. <https://doi.org/10.1063/1.438980>.
- [89] P.C. Hariharan, J.A. Pople, The influence of polarization functions on molecular orbital hydrogenation energies, *Theoret. Chim. Acta* 28 (1973) 213–222. <https://doi.org/10.1007/BF00533485>.
- [90] T. Clark, J. Chandrasekhar, G.W. Spitznagel, P.V.R. Schleyer, Efficient diffuse function-augmented basis sets for anion calculations. III. The 3-21+G basis set for first-row elements, Li–F, *Journal of Computational Chemistry* 4 (1983) 294–301. <https://doi.org/10.1002/jcc.540040303>.
- [91] S. Grimme, J. Antony, S. Ehrlich, H. Krieg, A consistent and accurate ab initio parametrization of density functional dispersion correction (DFT-D) for the 94 elements H–Pu, *J Chem Phys* 132 (2010) 154104. <https://doi.org/10.1063/1.3382344>.
- [92] J.B. Birks, L.G. Christophorou, Excimer fluorescence spectra of pyrene derivatives, *Spectrochimica Acta* 19 (1963) 401–410. [https://doi.org/10.1016/0371-1951\(63\)80051-X](https://doi.org/10.1016/0371-1951(63)80051-X).

- [93] P.R. Salvi, E. Castellucci, P. Foggi, R. Quacquarelli, Vibronic coupling of pyrene in the first $\pi\pi^*$ excited state, *Chemical Physics* 83 (1984) 345–356. [https://doi.org/10.1016/0301-0104\(84\)85010-7](https://doi.org/10.1016/0301-0104(84)85010-7).
- [94] W. Karcher, ed., *Spectral Atlas of Polycyclic Aromatic Compounds*, Springer Netherlands, Dordrecht, 1988. <https://doi.org/10.1007/978-94-009-1263-2>.
- [95] F. Cignoli, S. Benecchi, G. Zizak, D. Tencalla, *Atlas of fluorescence of spectra of aromatic hydrocarbons*, Ed. S. D. Iuliiis and D. Ferretti, Editorial Group & Graphic Design (1992).
- [96] B.A. Kirsch, J.D. Winefordner, Electrothermal vaporization and laser-induced fluorescence for screening of polyaromatic hydrocarbons, *Anal. Chem.* 59 (1987) 1874–1879. <https://doi.org/10.1021/ac00141a031>.

Appendices:

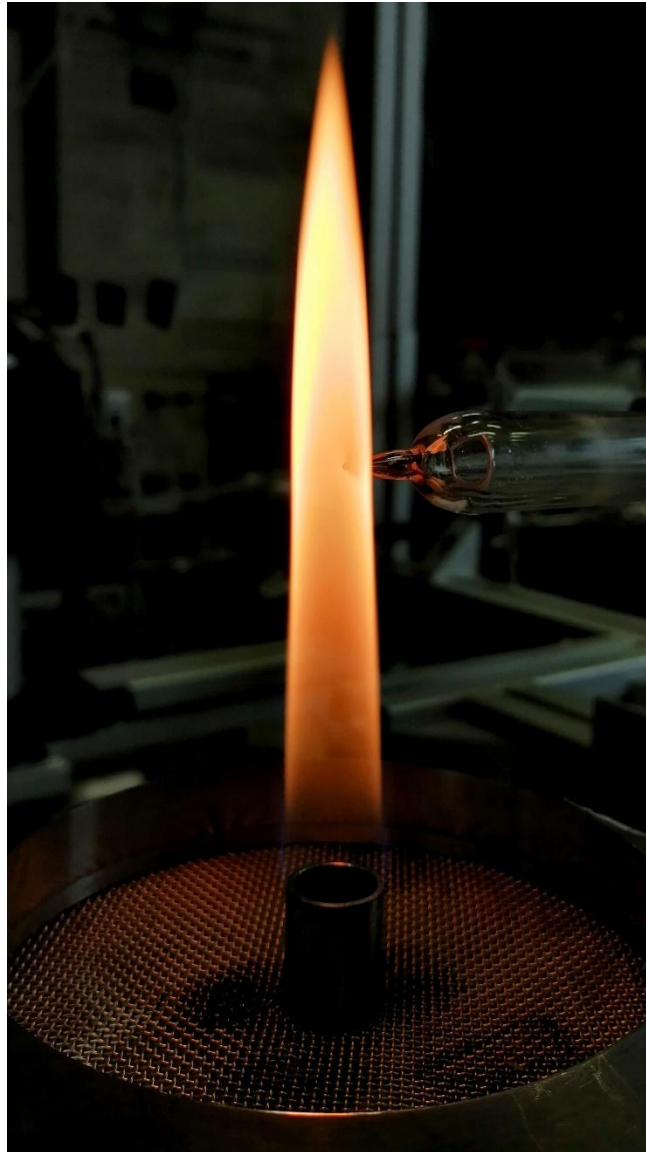


Figure A.1: Pictures of the investigated laminar diffusion methane flame with a sampling probe (not used in this work).

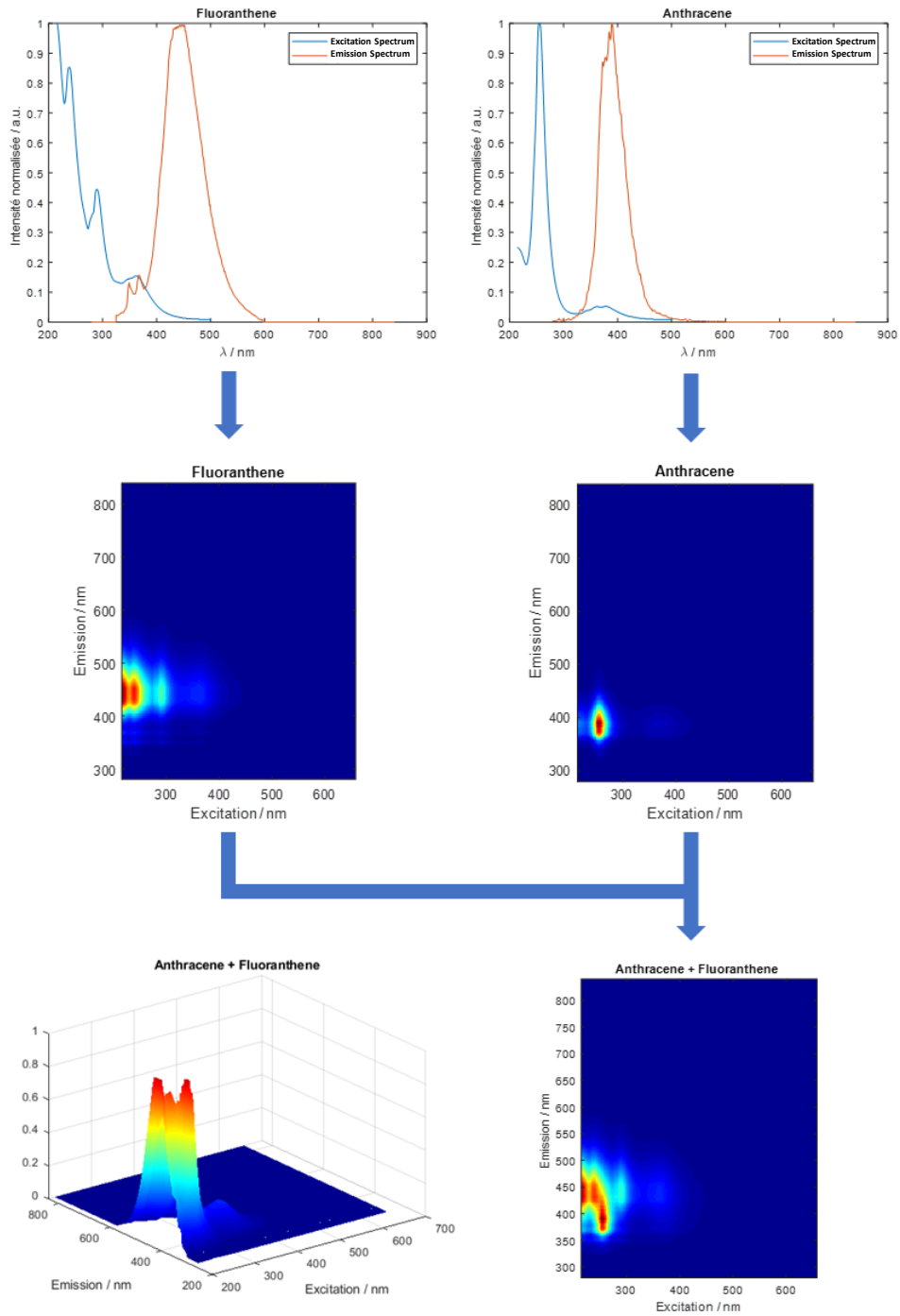
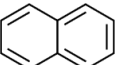
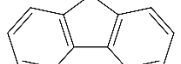
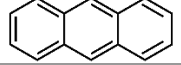
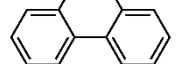
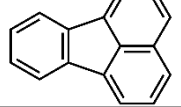
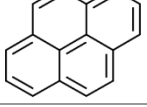
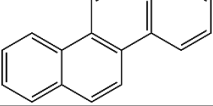
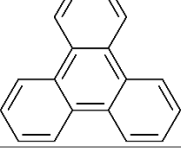
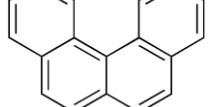
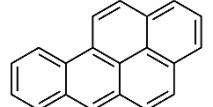
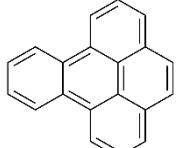
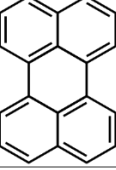


Figure A.2: Illustration of the EEM fluorescence spectra construction process for anthracene, fluoranthene, and their mixture based on the reference spectra reported in table A.1

PAHs	Molecular Formula	Structure	Excitation Spectrum	Emission Spectrum
Naphthalene	C ₁₀ H ₈		Bauer et al. [55]	Orain et al. [60]
9H-fluorene	C ₁₃ H ₁₀		Bauer et al. [55]	Karcher et al. [94]
Anthracene	C ₁₄ H ₁₀		Bauer et al. [55]	Cignoli et al. [95]
Phenanthrene	C ₁₄ H ₁₀		Bauer et al. [55]	Cignoli et al. [95]
Fluoranthene	C ₁₆ H ₁₀		Bauer et al. [55]	Ledier [61]
Pyrene	C ₁₆ H ₁₀		Bauer et al. [55]	Cignoli et al. [95]
Chrysene	C ₁₈ H ₁₂		Bauer et al. [55]	Kirsch et al. [96]
Triphenylene	C ₁₈ H ₁₂		Bauer et al. [55]	Karcher et al. [94]
Benzo[c]phenanthrene	C ₁₈ H ₁₂		Bauer et al. [55]	Karcher et al. [94]
Benzo[a]pyrene	C ₂₀ H ₁₂		Bauer et al. [55]	Cignoli et al. [95]
Benzo[e]pyrene	C ₂₀ H ₁₂		Bauer et al. [55]	Karcher et al. [94]
Perylene	C ₂₀ H ₁₂		Bauer et al. [55]	Cignoli et al. [95]

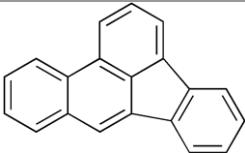
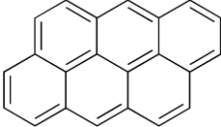
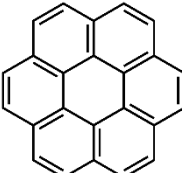
Benzo[b]fluoranthene	$C_{20}H_{12}$		Bauer et al. [55]	Karcher et al. [94]
Anthanthrene	$C_{22}H_{12}$		Bauer et al. [55]	Karcher et al. [94]
Coronene	$C_{24}H_{12}$		Bauer et al. [55]	Cignoli et al. [95]

Table A.1: PAHs considered for the construction of the reference EEM matrices and the corresponding references for the absorption and emission spectra.